Journal of Photochemistry & Photobiology A: Chemistry 364 (2018) 219–232

Contents lists available at ScienceDirect

Journal of Photochemistry & Photobiology A: Chemistry

journal homepage: www.elsevier.com/locate/jphotochem

Cost-effective and dynamic carbon dioxide conversion into methane using a $CaTiO_3$@Ni-Pt catalyst in a photo-thermal hybrid system

Jae Hyung Lee[a], Jeong Yeon Do[a,*], No-Kuk Park[b], Myung Won Seo[c], Ho-Jung Ryu[c], Jin-Pyo Hong[d], Yang Soo Kim[e], Seog. K. Kim[a], Misook Kang[a,*]

[a] Department of Chemistry, College of Natural Sciences, Yeungnam University, Gyeongsan, Gyeongbuk 38541, Republic of Korea
[b] School of Chemical Engineering, Yeungnam University, Gyeongsan, Gyeongbuk 38541, Republic of Korea
[c] Korea Institute of Energy Research, 152 Gajeong-ro, Yuseong-gu, Daejeon 34129, Republic of Korea
[d] Korea Electric Power Corporation Research Institute, 105 Munji-ro, Yuseong-gu, Daejeon 34056, Republic of Korea
[e] Jeonju Center, Korea Basic Science Institute, Jeonju, Jeonbuk 54907, Republic of Korea

ARTICLE INFO

Keywords:
$CaTiO_3$/Ni/Pt
Photo-thermal hybrid system
CO_2 methanation
CH_4 selectivity

ABSTRACT

This research focuses on the synergy of converting carbon dioxide (CO_2) into methane (CH_4) by simultaneously introducing light and heat as dynamic sources to activate the catalyst. A $CaTiO_3$@Ni-Pt catalyst, loaded with 30.0 wt.% Ni and 1.0 wt.% Pt on a perovskite $CaTiO_3$ support was introduced. The photo-thermal catalytic hybrid system has two features that distinguish it from other photo- or thermal-catalytic systems. First, unlike the CO_2 thermal-methanation reaction where CO_2 and H_2 react at a molar ratio of 1:4, 2.0 mol of H_2 was replaced with 2.0 mol H_2O in the photo-thermal catalytic hybrid system compared to the thermal-methanation reaction requiring 4.0 mol of H_2. Second, by loading Ni and Pt, which are catalytic active species with excellent CO_2 and H_2 adsorption abilities, the CO_2 reduction (46.48%) was promoted and the CH_4 selectivity (99.46%) in the product was increased compared to the photo-methanation reaction. The $CaTiO_3$@Ni-Pt not only inhibited the recombination of the photo-generated charges, but also facilitated the adsorption of the reactants in the photo-thermal hybrid system. The quantum efficiency of the $CaTiO_3$@Ni-Pt catalyst measured for the photo-thermal hybrid system steadily increased to 180 °C. Nevertheless, this study implies that a photo-thermal hybrid system can be useful to photo-reducing CO_2 by adding a small amount of heat. From a thermal reaction standpoint, a photo-thermal hybrid system can be used to reduce the reaction temperature during CO_2 thermal-methanation and to reduce the consumption of H_2 in half.

1. Introduction

Recently, carbon dioxide (CO_2) emissions in the atmosphere have increased significantly as consumption of fossil fuels continues to grow along with the energy demands. Since CO_2 is the main cause of global warming, and as a result, environmental pollution problems such as climate change on Earth arise, the world is paying keen attention to measures meant to reduce greenhouse gases. Carbon capture and storage (CCS) was used in the past to reduce CO_2 emissions, but due to storage space and cost issues, research into carbon capture and utilization (CCU) is receiving increasing attention these days [1,2]. The conversion of CO_2 to renewable hydrocarbon fuels for recycling is an attractive solution to address both energy and environmental issues at the same time. Until now, there are two well-known fuel production methods using CO_2 conversion: photocatalytic and thermochemical CO_2 conversion. Photocatalytic CO_2 conversion [3] produces renewable fuels such as methane (CH_4) through the reduction of CO_2 with H_2O based on the following equation:

$$CO_2 + 2H_2O + h\nu \rightarrow CH_4 + 2O_2 \ (E_{redox} = -0.24\ eV) \quad (1)$$

This method is expected to be sustainable and environmentally friendly since it uses solar light. Although many researchers are working hard to develop new photocatalysts for the production of solar fuel, there are limitations in the relatively low charge separation efficiency of semiconductors and selectivity of reduction [4]. Furthermore, another important CO_2 thermochemical conversion method is the so-called Sabatier reaction [5], which is the hydrogenation of CO_2 for CH_4 production as shown in Eq. (2):

$$CO_2 + 4H_2 \rightarrow CH_4 + 2H_2O \ (\Delta H^{\circ}_{298\ K} = -165\ kJ/mole) \quad (2)$$

This is one of the simplest catalytic CO_2 hydrogenation techniques and a promising way to reduce CO_2 using H_2 obtained from the

* Corresponding authors.
E-mail addresses: daengi77@ynu.ac.kr (J.Y. Do), mskang@ynu.ac.kr (M. Kang).

https://doi.org/10.1016/j.jphotochem.2018.05.045
Received 13 April 2018; Received in revised form 21 May 2018; Accepted 29 May 2018

electrolysis of water. Although it is a favorable exothermic reaction with high CH_4 production rate in the 200–550 °C temperature range, the reaction rate is limited due to the high motion barrier of the eight-electron reduction process [6]. To overcome the limitations of these two methods, a solar fuel production method based on the photo-thermal effect has recently been proposed as a new alternative. The photo-thermal catalytic reaction is an effective method of fueling CO_2, which can achieve high thermo-catalytic efficiency by taking advantage of the photocatalyst using solar energy [7]. By locally heating the catalyst, photo-thermal effects can be induced as the photon energy is rapidly converted into heat [8]. In particular, photo-thermal hybrid catalysts are advantageous as they have higher electron density due to light absorption and reactant adsorption sites and higher efficiency than conventional semiconductor photocatalysts [9].

Therefore, in this study, we have attempted to develop a catalyst that can be applied to a novel photo-thermal hybrid system with high CO_2 conversion at low temperatures by improving the existing photocatalyst. In the Sabatier reaction, the molar ratio of CO_2 to H_2 is 1:4. We expected a synergistic effect of the photo-thermal effect and the photoreduction of CO_2 by substituting some H_2 with H_2O. Water is an attractive, cost effective H_2 source. In general, nano-metals such as Au [10], Ag [11], and Pd [12] have been studied in various fields, such as oxidation or reduction of organic pollutants, due to their strong Surface Plasmon Resonance (SPR) effects. However, since they are expensive, they are disadvantageous. Therefore, we have sought a new high efficiency CO_2 fuel photo-thermal catalyst by using a relatively low-cost transition metal (Ni) and a very small amount of noble metal (Pt) on a perovskite-type semiconductor support. The top priority for the catalytic design was to find a composition that would be favorable for the adsorption and target activation of CO_2 and H_2. First, we focused on CO_2 adsorption and used perovskite $CaTiO_3$ with an ABO_3 formula as support. Calcium is a representative material used for CCS, and is well known for its excellent ability to absorb CO_2 [13]. In addition, perovskite-type catalysts have attracted significant interest as photocatalysts since they have unique characteristics, various structural phase transitions, and their composition can be changed [14]. For the high conversion and selectivity of the CO_2 methanation reaction, we loaded 30.0 wt.% Ni and 1.0 wt.% Pt on a $CaTiO_3$ support. Nickel is a representative transition metal that is advantageous for the direct hydrogenation of CO_2, as already proved in several studies [15,16]. Here, we added a small amount of Pt as co-catalyst. Panagiotopoulou et al. [17] have reported that noble metal nanoparticles such as Ru and Rh are highly efficient thermal or photo-thermal catalysts for activating H_2. Furthermore, using noble metal particles is also a strategy for suppressing the recombination of photogenerated charges and improving the utilization efficiency of the photogenerating electrons in the optically active portion. Therefore, we selected Pt as a noble metal since it can easily adsorb H_2, and expected that Pt nanoparticles could rapidly increase the local temperature under light irradiation, thus activating H_2 and promoting CO_2 hydrogenation [18].

Eventually, three types of $CaTiO_3$ catalysts were prepared in this study: pure $CaTiO_3$, 70.0 wt.% $CaTiO_3$/30.0 wt.% Ni ($CaTiO_3$@Ni) and 70.0 wt.% $CaTiO_3$/30.0 wt.% Ni/1.0 wt.% Pt ($CaTiO_3$@Ni-Pt), and 0.2 g of each catalysts was coated on a glass bead to facilitate the CO_2 photo-thermal hybrid reaction. The physical properties of these catalysts were confirmed using various methods.

2. Experimental

2.1. Preparation of $CaTiO_3$, $CaTiO_3$@Ni, and $CaTiO_3$@Ni-Pt nanoparticles

We synthesized $CaTiO_3$ nanoparticles using a typical sol-gel method [19]. The molar ratio of Ca:Ti:citric acid was adjusted to 1:1:6, and the specific synthesis procedure was as follows. To prepare the Ca aqueous solution, 17.71 g calcium nitrate tetra-hydrate ($Ca(NO_3)_2{\cdot}4H_2O$, 99.99%, Junsei Chem., Japan) was dissolved in 150 mL distilled water, and then 11.5 mL nitric acid (HNO_3, 60.0%, Junsei Chem., Japan) was slowly added to the solution. Subsequently, we prepared a Ti aqueous solution with the same molar ratio as Ca. We dissolved 21.32 g titanium iso-propoxide (TTIP, $Ti[OCH(CH_3)_2]_4$, 98.0%, Junsei Chem., Japan) in 150 mL absolute ethanol, and then we added 11.5 mL acetic acid (CH_3COOH, 99.85%, Junsei Chem., Japan) to the solution. The above two aqueous solutions were mixed while stirring for 2 h. Furthermore, 94.56 g citric acid ($C_6H_8O_7$, 98%, Junsei Chem., Japan) was added to the mixed solution, and the solution was further stirred for 2 h. Subsequently, the mixed solution was evaporated at 200 °C and dried at 80 °C for 12 h. The resulting powder was then heat-treated at 600 °C for 6 h, generating white $CaTiO_3$ nanoparticles.

To prepare $CaTiO_3$@Ni nanoparticles, the prepared $CaTiO_3$ was used as support and 30.0 wt.% Ni was deposited using the following impregnation method [20]. We suspended 70.0 wt.% $CaTiO_3$ in absolute ethanol (C_2H_5OH, 99.8%, Junsei Chem., Japan) and stirred for 1 h. To this solution, we added $Ni(NO_3)_2$ to reach 30.0 wt.% NiO, and the solution was further stirred for 2 h. The solvent was evaporated at 80 °C for 3 h. The dried powder was heat treated at 500 °C for 2 h to form NiO crystals, thus ensuring a good attachment of the catalyst species to the support and the removal of impurities. The color of the powder thus obtained was gray.

We used platinum (IV) chloride ($PtCl_4$, 99.99%, Junsei Chem., Japan) as a precursor of Pt to prepare the $CaTiO_3$@Ni-Pt nanoparticles. 1.0 wt.% Pt was added to the obtained 70.0 wt.% $CaTiO_3$/30.0 wt.% Ni following the same procedure described above except for the weight content. The color of the $CaTiO_3$@Ni-Pt powder thus obtained was black-gray.

2.2. Characterizations of $CaTiO_3$, $CaTiO_3$@Ni, and $CaTiO_3$@Ni-Pt nanoparticles

The prepared $CaTiO_3$, $CaTiO_3$@Ni, and $CaTiO_3$@Ni-Pt catalysts were examined using powder X-ray diffraction (XRD) patterns (MPD, PANalytical) to verify their crystallinity and structure. We performed measurements using Cu Kα (λ = 1.5056 Å) radiation (40 kV, 30 mA) filtered with Ni in the 2θ = 20–100° range. The morphology of the $CaTiO_3$@Ni-Pt catalyst was analyzed using high resolution transmission electron microscopy (TEM, H-7600, Hitachi). In addition, the overall shape of the particles was confirmed using scanning electron microscopy (SEM, S-4100, Hitachi), and the element composition of each catalyst was confirmed using energy dispersive spectrometry (EDS, EX-250, Horiba) analysis. The diffuse reflectance spectra of the $CaTiO_3$, $CaTiO_3$@Ni, and $CaTiO_3$@Ni-Pt catalysts were obtained using a UV–vis spectrophotometer (Neosys-2000, SCINCO) to confirm their optical properties. To confirm the oxidation states of the Ca2p, Ti2p, O1s, Ni2p, and Pt2f components of all the catalysts, an AXIS-Nova spectrometer (Kratos Inc.) equipped with a monochromatic Al*K*α (1486.6 eV) X-ray source was used to obtain the X-ray photoelectron spectroscopy (XPS) images. The XPS signals were fitted using mixed Lorentzian-Gaussian curves.

The photocurrent measurements of the catalysts confirmed the efficiency of separation between the photo-generated electrons and holes pairs (e^-/h^+), and photoluminescence (PL, Perkin Elmer) spectroscopy of the powdered catalysts was used to determine their recombination propensity. We used the same 150 W continuous Xenon lamp light source for these measurements. The photocurrent densities were measured utilizing a two electrode system using a platinum wire as a counter electrode after coating the particles on fluorine-doped tin oxide (FTO) glass. The photocurrent value was measured when the light was irradiated onto a predetermined unit area of the catalyst at 30 s intervals. The optical efficiency could be estimated based on the measured photocurrent value using a Sun 2000 solar simulator (Ivium Stat, Abet technologies) with a red light-emitting diode (max. wavelength = 620 nm). The quantum efficiencies of the catalysts were measured by irradiating them using light and heat under the same

conditions for the CO_2 photo-thermo hybrid reaction using the same two electrode system to measure the photocurrent.

2.3. Gas adsorption abilities of $CaTiO_3$, $CaTiO_3$@Ni, and $CaTiO_3$@Ni-Pt nanoparticles

The Brunauer-Emmett-Teller (BET) surface areas of the $CaTiO_3$, $CaTiO_3$@Ni, and $CaTiO_3$@Ni-Pt catalysts were obtained from liquid nitrogen-adsorption/desorption isotherm curves measured using a Belsorp II instrument (Belsorp II mini, Japan). Water and impurities were removed by pretreatment at 200 °C for 1 h.

The temperature programmed desorption (TPD) of CO_2 was measured using a BELCAT (Bel Japan Inc., Japan) catalyst analyzer to compare the adsorption capacities of the catalysts for CO_2 gas. The catalysts were pretreated at 300 °C for 1 h under He flow to remove the physically absorbed water and impurities. Subsequently, each catalyst was used to adsorb CO_2 gas (5 vol.% CO_2/He) at 50 °C under 50 mL min^{-1} flow for 1 h. The desorbed CO_2 gas was detected using a TCD detector while increasing the temperature from 50 to 600 °C at a 10 °C min^{-1} rate under He flow. The H_2 temperature-programmed reduction (TPR) experiments were conducted using the same equipment as the TPD experiments (Bel Japan Inc., Japan).

2.4. Carbon dioxide photo-thermal conversion over $CaTiO_3$, $CaTiO_3$@Ni, and $CaTiO_3$@Ni-Pt catalysts

A fixed-bed reactor as shown in Fig. 1 was used for the CO_2 photo-thermal reaction. The catalytic activity was measured by reacting CO_2, H_2, and H_2O at a molar ratio of 1:2:2 at 40–240 °C for 1 h at 40 °C intervals. The catalyst (0.2 g) was coated on a glass bead, packed in a fixed bed quartz reactor, and mounted vertically. All catalysts were reduced under H_2 flow (10 mL/min) for 1 h at 500 °C before each run. In this study, UV lamps (365 nm, 9 W/cm^2) were placed outside the quartz tube for the photo-thermal hybrid reaction and packed in a furnace. The amount of H_2O vapor was controlled by adjusting the temperature according to the partial pressure law [21]. The CO_2 photo-thermal hybrid reaction was performed at a 3000 h^{-1} gas hourly space velocity (GHSV), and the most efficient photo-thermal hybrid reaction conditions were found after light and heat exposure for 1 h at 40 °C intervals between 40 and 240 °C. For comparison, the CO_2 fueling performance was also analyzed when the same catalysts were only irradiated using light (CO_2 photo-reduction reaction) and subsequently when only heat was applied (the Sabatier reaction). The reaction formulas in this study can be expressed as a mixed equation between the photo- and thermo-reaction as shown in the next Eq. (3):

$$CO_2 + 2H_2O + 2H_2 + \Delta + h\nu \rightarrow CH_4 + O_2 + 2H_2O \quad (3)$$

The gas produced during the CO_2 photo-thermal hybrid reaction was analyzed using an on-line gas chromatograph (DS7200, Donam Company, Korea) equipped with a thermal conductivity detector (TCD) and flame ionization detector (FID). A Carboxen-1000 column (Young Lin Instrumentals Co., Korea) was used to identify H_2, CO, and CO_2 in the TCD, while C_1-C_3 light hydrocarbons were detected using the FID. In this study, CO and CH_4 gases were formed as reaction products, and the selectivity for each gaseous product (X_{gas}) was calculated using Eq. (4). The conversion of CO_2 was calculated using Eq. (5) and the intermediates produced during the reaction were confirmed by mass analysis.

$$X_{gas}\ selectivity\ (\%) = \frac{[X_{gas}]_{out}}{\sum [all\ gases]_{out}} \times 100\% \quad (4)$$

$$CO_2\ \text{conversion}\ (\%) = \frac{[CO_2]_{in} - [CO_2]_{out}}{[CO_2]_{in}} \times 100\% \quad (5)$$

3. Results and discussion

3.1. Physicochemical properties of the $CaTiO_3$, $CaTiO_3$@Ni, and $CaTiO_3$@Ni-Pt catalysts

To confirm the crystallinity of the synthesized $CaTiO_3$, $CaTiO_3$@Ni, and $CaTiO_3$@Ni-Pt catalysts before the reaction, we used their XRD patterns as shown in Fig. 2(A). The $CaTiO_3$ samples without Ni and Pt loading showed orthorhombic perovskite structure [JCPDS card no. 01-

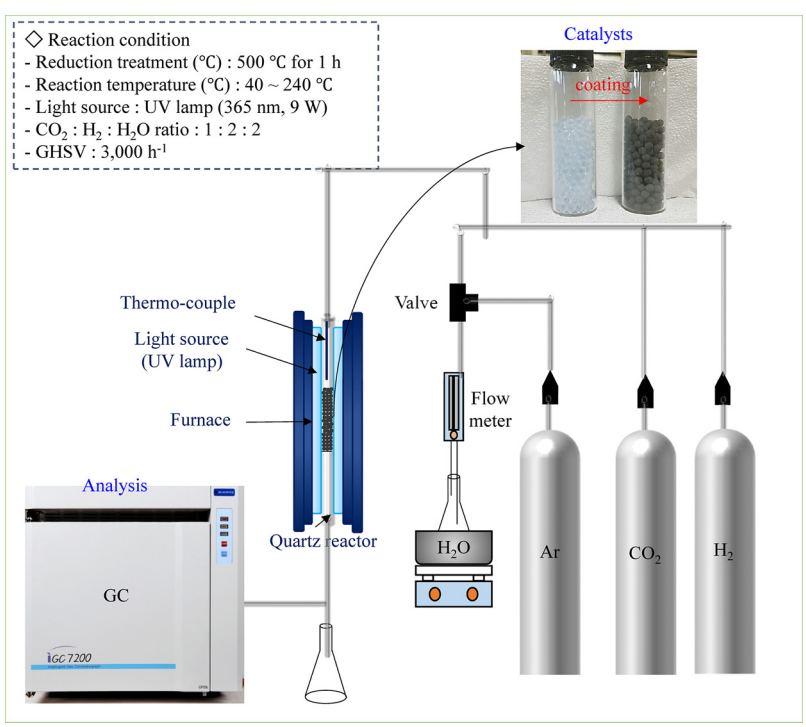

Fig. 1. Reactor for the CO_2 photo-thermal hybrid reaction.

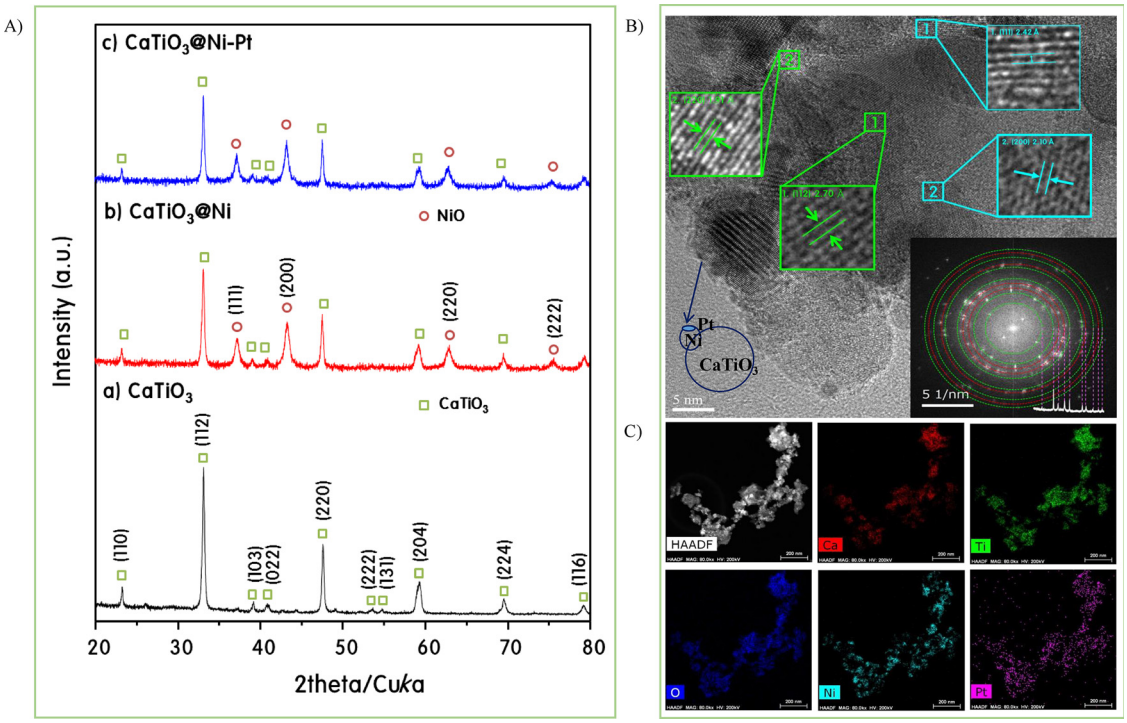

Fig. 2. (A) XRD patterns of all catalysts, (B) HRTEM and SAED images, and (C) element mapping image of $CaTiO_3$@Ni-Pt.

078-1013]. The main XRD peaks for $CaTiO_3$ were 2θ = 23.23° (110), 33.11° (112), 39.10° (103), 40.68° (022), 47.49° (220), 53.53° (222), 54.69° (131), 59.04° (024), 69.49° (224), and 79.22° (116) [22]. The XRD patterns of the $CaTiO_3$/Ni samples showed only $CaTiO_3$ and NiO peaks and no additional impurities peaks. The main peaks corresponding to the (111), (200), (220) and (222) crystal planes of NiO [23] were observed at 2θ = 37.24, 43.29, 62.92, and 75.41°, respectively, similar to perovskite $CaTiO_3$. In addition, of the amount of Pt in the $CaTiO_3$@Ni-Pt sample loaded with 1.0 wt.% Pt was too small to detect a Pt related peak. Comparing the XRD patterns of all samples, there was no apparent peak shift overall, but there were differences in peak intensities and widths, which can be explained in relation to the crystal size. The crystallite sizes of the $CaTiO_3$, $CaTiO_3$@Ni and $CaTiO_3$@Ni-Pt particles were calculated using Scherer's equation [24] to be 28.6, 27.6, and 25.9 nm, respectively. To investigate the intrinsic crystal structure and elemental dispersion of $CaTiO_3$@Ni-Pt particles, Fig. 2(B) and (C) show a high resolution TEM image, a selected region electron diffraction pattern, and an elemental mapping image. Generally, when a point in the selected area electron diffraction (SAED) pattern has a certain interval, it implies the presence of a single crystal, while polycrystalline structures are associated with continuous rings [25]. The $CaTiO_3$@Ni-Pt particles demonstrate a polycrystalline structure with a partially defined diffraction spot and a ring pattern together. As shown in Fig. 2(B), the $CaTiO_3$@Ni-Pt particles are expected to be aggregates of single crystals with different orientations. The grating pattern for 2.70 Å (112) and 1.91 Å (220) corresponds to orthorhombic $CaTiO_3$, while 2.42 Å (111) and 2.10 Å (220) were in good agreement with rhombohedral NiO. Meanwhile, Fig. 2(C) shows that Ca, Ti, O, Ni, and Pt were uniformly distributed throughout the $CaTiO_3$@Ni-Pt particles, and that the Pt loaded at the end was located at the outermost surface. Thus, it can be seen that a large $CaTiO_3$ circle was located in the center of the sample, and the NiO had a smaller elliptical shapes and partially covered $CaTiO_3$, while small doted Pt was dispersed throughout the entire sample. It should be noted that these were the expected characteristics for $CaTiO_3$@Ni-Pt.

Fig. 3 shows the SEM images and EDS patterns of the $CaTiO_3$, $CaTiO_3$@Ni, and $CaTiO_3$@Ni-Pt particles. $CaTiO_3$ has slightly agglomerated particles and irregular morphology. Moreover, the SEM images of the $CaTiO_3$@Ni and $CaTiO_3$@Ni-Pt particles show less cohesion and smaller particles than $CaTiO_3$. This indicates that Ni and Pt are contained between the Ca and Ti components, preventing their strong aggregation. We also performed EDS analysis to determine the chemical composition of the catalyst. The peak of the spectrum showed only the presence of Ca, Ti, O, Ni and Pt. The atomic content of each sample is summarized in Table. The Ca:Ti atomic ratio in the $CaTiO_3$ sample was approximately 1:1, indicating that the sample was stoichiometrically well synthesized. In addition, the amounts of added Ni and Pt were determined to be 31.91 and 1.11% by mass ratio, respectively, similar to the amounts actually added. In particular, the addition of Ni and Pt reduced the atomic ratio of Ca and Ti, and the amount of atoms exposed on the catalyst surface was different for each sample. Generally, the amount of catalytically active species exposed on the catalyst surface was closely related to the catalytic performance [26], and the more exposed main catalytic amount, the better the catalyst performance.

3.2. Optical properties of the $CaTiO_3$, $CaTiO_3$@Ni, and $CaTiO_3$@Ni-Pt catalysts

Before evaluating the CO_2 photo-thermal hybrid reaction, the UV–vis absorption curve and the Tauc plots in Fig. 4 can help understand the optical characteristics of the catalysts. In general, the optical properties of a catalyst are closely related to their photocatalytic performance, and fine changes can be predicted according to the chemical characteristics of the particle surface [27]. Fig. 4(A) shows the UV–vis absorption curves of all catalysts. The $CaTiO_3$ particle was white and exhibited strong absorption in the UV region below 400 nm. However, $CaTiO_3$@Ni and $CaTiO_3$@Ni-Pt were dark gray, and the absorption spectra extended into the visible range. In the UV region, a response similar to $CaTiO_3$ was recorded, but the absorption edge was slightly shifted toward the long wavelength side and the sample exhibited high absorption in the visible light region. These results can be attributed to the 3d Ni excitation and/or the 5d Pt electrons jumping from the transition metal valence band (VB) to the $CaTiO_3$ conduction band (CB)

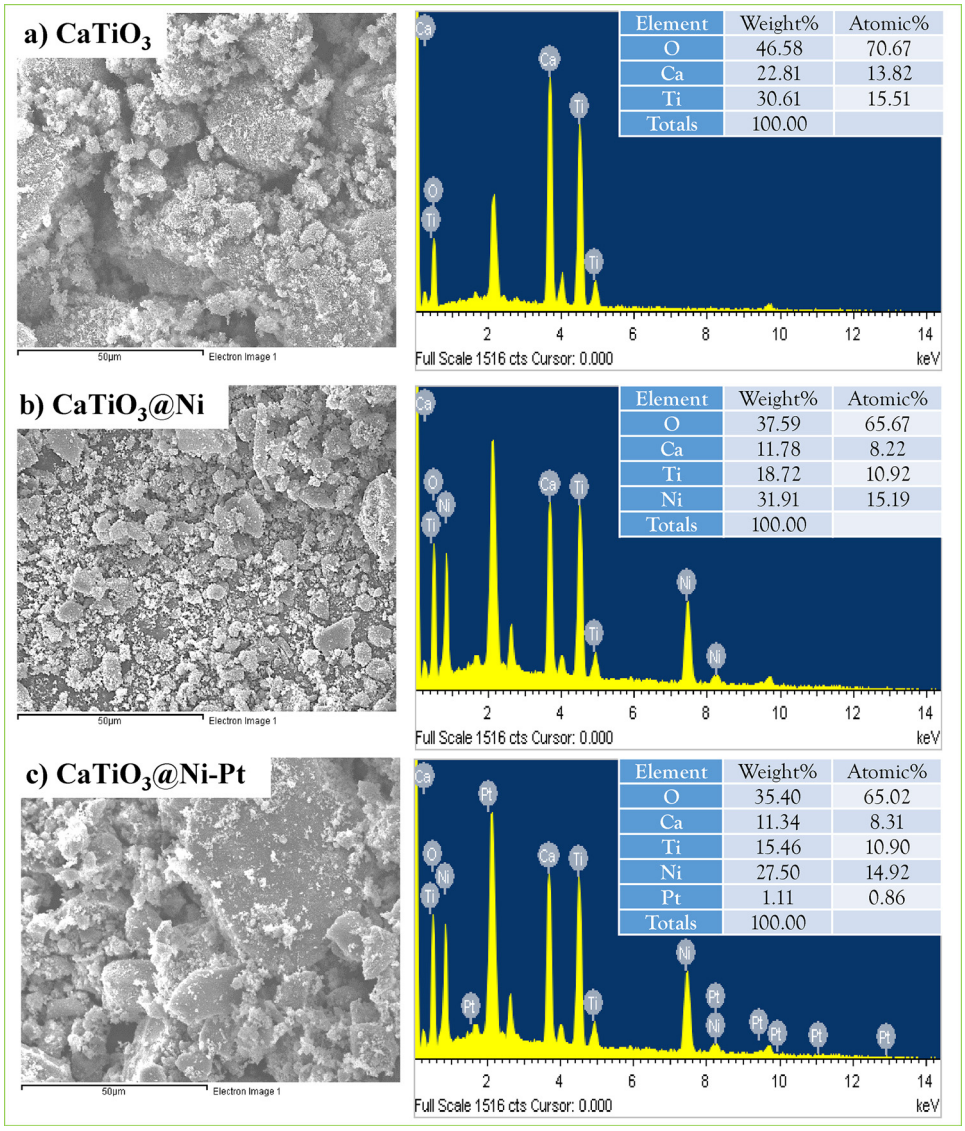

Fig. 3. SEM images and EDS curves of $CaTiO_3$, $CaTiO_3$@Ni, and $CaTiO_3$@Ni-Pt.

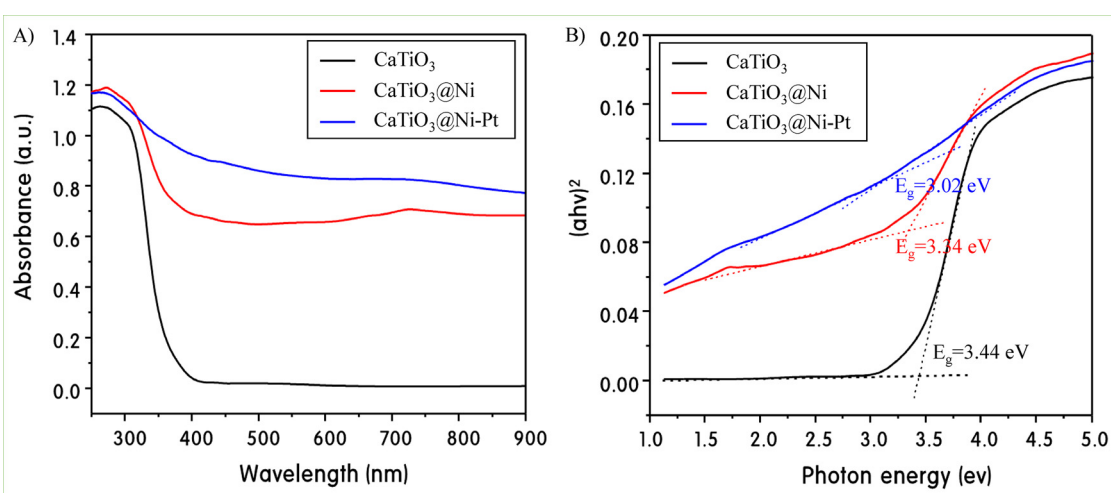

Fig. 4. (A) UV–vis spectroscopy curves and (B) Tauc plots of $CaTiO_3$, $CaTiO_3$@Ni, and $CaTiO_3$@Ni-Pt.

[28]. Usually, the wavelength range of the light absorbed by semiconducting materials is related to the band-gap. When longer wavelengths are absorbed, the band-gap decreases [29]. Thus, the band-gap was calculated using the Tauc equation [30], and the results are shown in Fig. 4(B). The band-gap E_g was calculated using the equation $(h\upsilon)^n = B(h\upsilon - E_g)$, where $h\upsilon$ is the photon energy, α is the absorption coefficient, B is a constant depending on the relative material, and the exponent n depends on the transitional nature (2 for direct allowed transitions, 2/3 for direct transposed states, and 1/2). The band-gaps of the $CaTiO_3$, $CaTiO_3$@Ni and $CaTiO_3$@Ni-Pt particles were calculated to be 3.44, 3.34 and 3.02 eV, respectively, when tangential lines were drawn from the UV absorption spectrum in the Tauc-type conversion graph. That is, the band-gap decreased as Ni and Pt were loaded. Wide band-gap semiconductors such as $CaTiO_3$ are largely dependent on excitation by UV radiation, which accounts for only 4% of the total solar energy. However, introducing Ni and Pt into $CaTiO_3$ lowered its band gap energy. It is anticipated that this would improve the absorptive capacity in the additional visible light region, promising a catalytic reaction, and enabling high utilization efficiency of solar energy due to strong absorption.

3.3. Gas adsorption ability of the $CaTiO_3$, $CaTiO_3$@Ni, and $CaTiO_3$@Ni-Pt catalysts

Xianguang et al. reported that nano-metals have a stronger light absorption effect than conventional semiconductor photocatalysts and exhibit a strong photo-thermal synergy effect [31]. The catalytic reaction efficiency varied depending on the oxidation state of the metal in other studies. Additionally, for the CO_2 thermal-methanation, the reduced catalyst showed better performance than the one that was not reduced [32]. Therefore, in this study, H_2-TPR of all catalysts was also used to determine the appropriate reduction temperature for the samples prior to the CO_2 photo-thermal hybrid reaction. Fig. 5(A) shows the H_2-TPR profile of the catalysts. For H_2-TPR, the peak area generally corresponds to the hydrogen uptake and the peak position refers to the reduction temperature of the catalytic species [33]. The $CaTiO_3$@Ni catalyst was considered to be NiO reduced to metal Ni at approximately 300–550 °C [34]. Furthermore, the intensity of the peak of the $CaTiO_3$@Ni-Pt catalyst increased as the reduction peak moved toward lower temperatures. The Ni reduction peak shifted toward a lower temperature compared to the $CaTiO_3$@Ni catalyst, separated by two curves corresponding to slightly different oxidation states, which seems to be the effect of Pt. Here, Pt is in intimate contact with Ni species to promote the reduction of NiO. In particular, sharp, large peaks in the 200–300 °C range correspond to the reduction of Pt oxide to metallic Pt [35]. Thus, there are many Pt sites exposed on the surface which can be considered very advantageous for H_2 adsorption. According to the results of H_2-TPR, Ni and Pt, which are the main catalyst species except for $CaTiO_3$ used as support, can be completely reduced at 550 °C. Therefore, all the catalysts were reduced at 550 °C for 1 h before the CO_2 photo-thermal reaction, and the XRD patterns of the catalysts after reduction are shown in Fig. 5(B). The pattern for $CaTiO_3$ was not significantly different before and after reduction, while $CaTiO_3$@Ni and $CaTiO_3$@Ni-Pt catalysts showed peaks corresponding to metallic Ni instead of NiO [JCPDS no. 01-070-1849]. The peaks were assigned to 2θ = 44.48° (111), 51.83° (200), and 76.35° (220) and correspond to a cubic crystal structure with an Fm-3 m space group [36].

The performance of a catalyst is closely related to its reactant adsorption capacity. Generally, the larger the surface area of a catalyst, the more the adsorption of the reactants increases and the catalyst performance can be improved [37]. Fig. 6 shows the N_2 adsorption-desorption isotherms of all catalysts at 77 K. Table 1 summarizes and compares the BET surface area and pore characteristics of the catalysts. According to IUPAC's isotherm classification standard, $CaTiO_3$ is a type II with almost no porosity [38]. Furthermore, $CaTiO_3$@Ni and $CaTiO_3$@Ni-Pt showed weak hysteresis loops at higher relative pressures being classified as type IV isotherms unlike $CaTiO_3$. This confirms the existence of bulk mesopores between the particles, and an increased surface area due to the addition of Ni and Pt. Some studies have reported that the addition of 0.5 wt.% or more of precious metal increases the catalyst surface area [39]. Consistent with those reports, the surface area was increased by Pt doping in this study, which was believed to be due to the increased pore volume of the catalyst.

In addition, the reactivity of the catalyst is strongly related to the adsorbing ability of the reactants or the intermediate gas. Thus, CO_2-TPD was performed to evaluate the degree of CO_2 bonding of the catalysts, and the results are shown in Fig. 7. First, the results of CO_2-TPD as metal oxide before the reduction treatment are shown in Fig. 7(A).

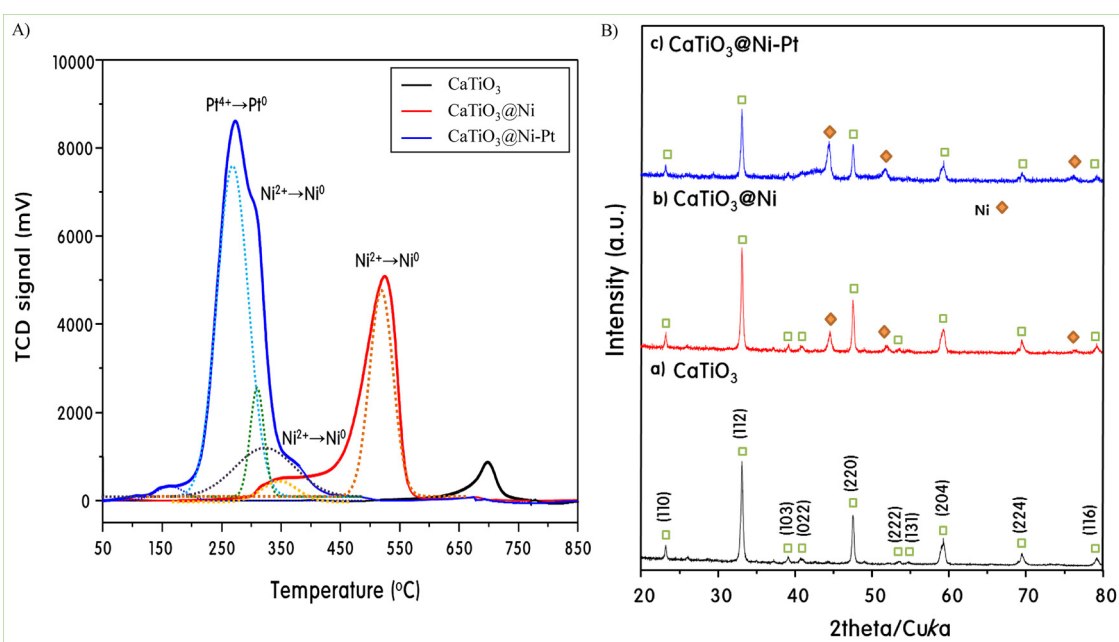

Fig. 5. (A) H_2-TPR profiles of $CaTiO_3$, $CaTiO_3$@Ni, and $CaTiO_3$@Ni-Pt before H_2 pre-treatment and (B) XRD patterns of $CaTiO_3$, $CaTiO_3$@Ni, and $CaTiO_3$@Ni-Pt after H_2 pre-treatment.

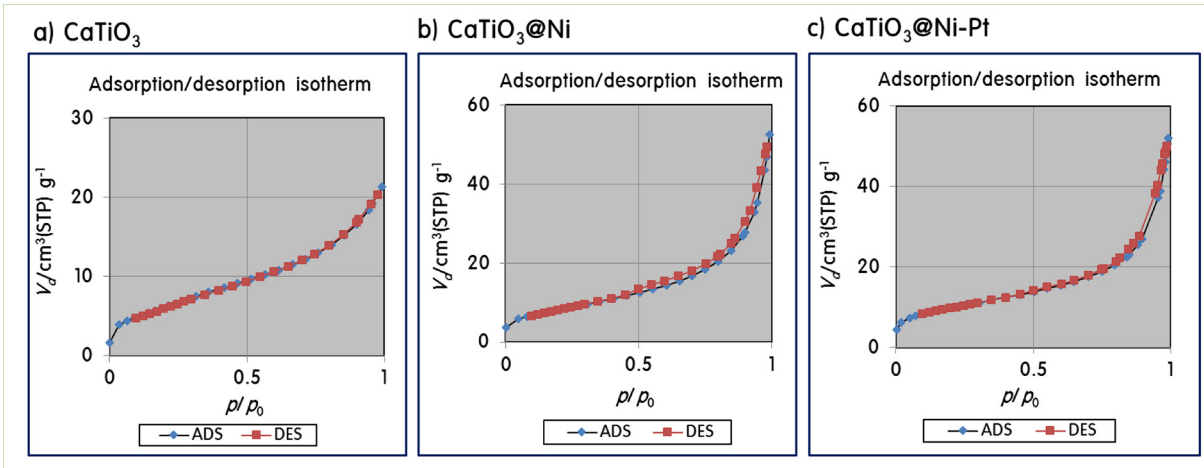

Fig. 6. Adsorption–desorption isotherm curves of N_2 at 77 K for $CaTiO_3$, $CaTiO_3$@Ni, and $CaTiO_3$@Ni-Pt.

Table 1
Textural properties of the $CaTiO_3$, $CaTiO_3$@Ni, and $CaTiO_3$@Ni-Pt catalysts obtained from the N_2 adsorption-desorption isotherms.

	$CaTiO_3$	$CaTiO_3$@Ni	$CaTiO_3$@Ni-Pt
V_m [cm^3(STP) g^{-1}]	5.38	6.86	7.69
$a_{s,BET}$ [m^2 g^{-1}]	23.42	29.86	33.49
Total pore volume (p/p_0 = 0.990) [cm^3 g^{-1}]	0.03	0.08	0.08
Mean pore diameter [nm]	5.61	10.70	9.40

$CaTiO_3$, which is already well known for its excellent CO_2 adsorption ability [40], can be also easily desorbed at low temperature. It is well known that CO_2 is a weak Lewis acid and can be adsorbed well to basic sites of metal oxides. The surface Lewis basicity of $CaTiO_3$ is increased by Ca, thus the availability of electrons necessary for CO_2 adsorption is increased. Furthermore, the adsorption of CO_2 on the $CaTiO_3$@Ni catalyst was decreased, because NiO covered the CO_2 adsorption sites on $CaTiO_3$. In addition, unlike $CaTiO_3$, $CaTiO_3$@Ni catalysts have two separate desorption peaks, which are believed to create new adsorption sites at the interface between the support and the metal. Meanwhile, the $CaTiO_3$@Ni-Pt catalyst showed stronger desorption peaks at lower temperatures compared to $CaTiO_3$@Ni. These results are attributed to the formation of new basic sites by Pt addition, led to improvements in the redox properties of the materials favoring oxygen transfer required for CO_2 activation. Fig. 7(B) shows the CO_2-TPD results after the reduction treatment for all catalysts. After the reduction pretreatment, the CO_2 desorption peaks of all catalysts were slightly shifted to lower temperatures, and their strengths were greatly increased. We concluded that a defect site was formed during the reduction of metal oxide to metal, and that site facilitated the adsorption of CO_2 [41].

3.4. Spectroscopic properties of the $CaTiO_3$, $CaTiO_3$@Ni, and $CaTiO_3$@Ni-Pt catalysts

We performed XPS measurements to investigate the chemical state of each ion in the $CaTiO_3$, $CaTiO_3$@Ni, and $CaTiO_3$@Ni-Pt catalysts. Fig. 8 shows the XPS spectra of Ca, Ti, O, Ni, and Pt for each catalyst. As can be seen, the Ca atomic spectra in $CaTiO_3$ were separated into two peaks, corresponding to $Ca2p_{1/2}$ and $Ca2p_{3/2}$ at 349.37 and 345.84 eV, respectively [42]. By the addition of Ni in the $CaTiO_3$@Ni catalyst, the chemical state of Ca migrated significantly toward higher binding energy, which means that the added Ni attracted the electrons of Ca to increase the oxidation state of Ca, and consequently oxygen defects (vacancies) can be expected in the crystal. When Pt coexisted here, the migration returned to low binding energy, but still showed a higher oxidation state than the Ca oxidation state in $CaTiO_3$. Furthermore, the addition of Pt significantly increased the $Ca2p_{1/2}$ peak area of HOMO, which means that there are many electrons in the HOMO orbital. In conclusion, regardless of the addition of Ni or Ni and Pt, the oxidation state of Ca in the $CaTiO_3$ crystals is greatly changed, and it is believed that $CaTiO_3$ perovskite structure defects such as oxygen vacancy have occurred. Also, we only observed two peaks corresponding to $Ti2p_{1/2}$

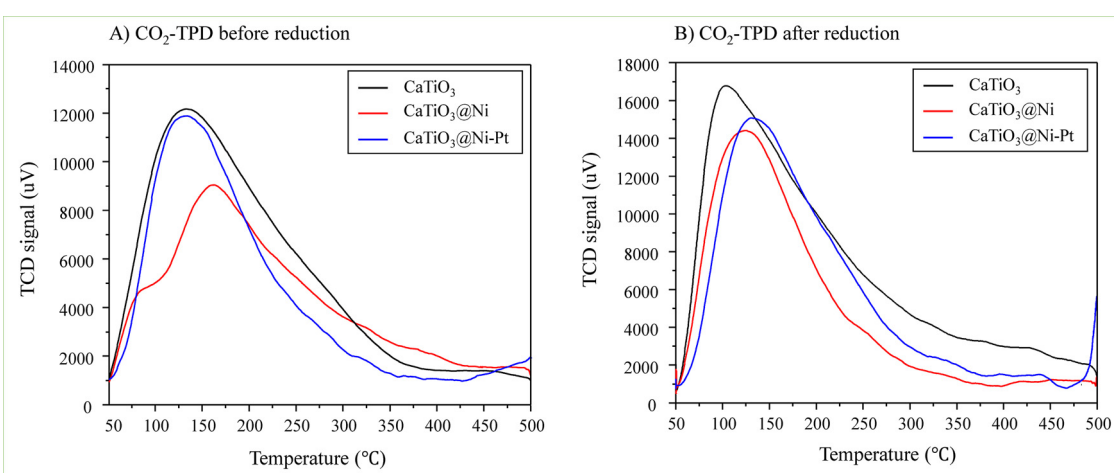

Fig. 7. CO_2-TPD curves of $CaTiO_3$, $CaTiO_3$@Ni, and $CaTiO_3$@Ni-Pt (A) before and (B) after H_2 pre-treatment.

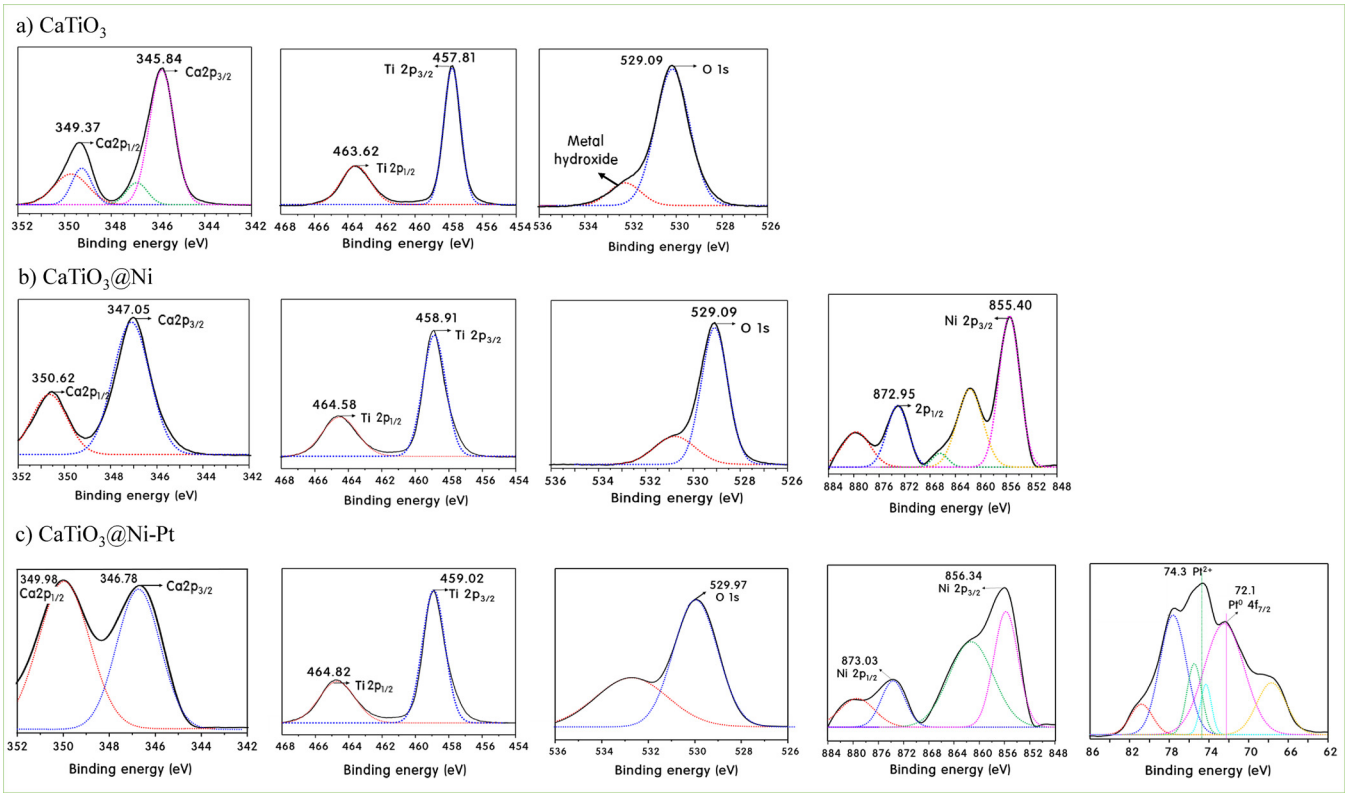

Fig. 8. XPS spectra of $CaTiO_3$, $CaTiO_3$@Ni, and $CaTiO_3$@Ni-Pt.

and $Ti2p_{3/2}$ in the Ti atom spectrum, thus, only Ti^{4+} was present in all catalysts. The binding energy of Ti shifted toward largely higher values in $CaTiO_3$@Ni and $CaTiO_3$@Ni-Pt compared to $CaTiO_3$. This may be related to the decrease in the electron density around the Ti atoms due to the interaction between Ti^{4+} and the loaded Ni or Pt [43]. Particularly, when Ni and Pt were added at the same time, Ti ion was more oxidized and moved to higher binding energy. The result could also expect that the oxidation state of Ti ions present in $CaTiO_3$ was also changed like Ca ions by Ni or Pt, and will be connected to oxygen vacancies in the $CaTiO_3$ perovskite structure. The photoelectron spectrum of the O1s electron showed the lattice oxygen of the catalyst and the oxygen of the OH group adsorbed on the surface. The main peak at 529.09 eV corresponded to the lattice oxygen, and the 531.04 eV peak was assigned to the non-lattice oxygen as oxygen in the surface OH group [44]. When Ni and Pt were loaded into $CaTiO_3$, the ratio of non-lattice oxygen increased, indicating oxygen defects in the lattice. The oxygen vacancies can act as reactant adsorption sites because they have properties that can be easily combined and stabilized with other atoms or groups. The XPS image of the loaded Ni2p was composed of two regions representing the spin levels of $Ni2p_{3/2}$ (855.40 eV) and $Ni2p_{1/2}$ (872.95 eV) [45]. Ancillary satellite peaks were observed, but all assigned peaks showed the presence of the Ni^{2+} cation in both catalysts of $CaTiO_3$@Ni and $CaTiO_3$@Ni-Pt. The absence of multiple segmentations of the peak corresponding to the oxidation state of Ni^{2+} demonstrated the formation of NiO. By the addition of Pt, the binding energy position shifted slightly higher, and the area of the peak was somewhat wider. From this result, it can be predicted that the Ni orbitals also have electron defects due to Pt. Meanwhile, the Pt was divided to two peaks, corresponding to $Pt4f_{7/2}$ of Pt in $CaTiO_3$@Ni-Pt, and there are Pt° at 72.1 eV and Pt^{2+} at 74.3 eV coexisted in different oxidation states [46].

It is very important to understand the optical properties of the catalyst in the photo-thermal hybrid reaction. Fig. 9 shows the PL spectra (A) and the photocurrent density results (B) of all catalysts. Fig. 9(A) shows the PL results when light with a maximum 325 nm excitation wavelength was applied. At 452 and 468 nm, the blue emission peaks appeared, which are related to the electron-hole pairs recombination promoted by high-energy defects. Generally, the lower the PL intensity, the more the recombination between the excited electrons and holes pairs was suppressed [47]. No new luminescence peaks due to the Ni and Pt dopants were observed and only the intensity decreased. According to Mehmood et al., Ni^{2+} used as a dopant can easily trap electrons with a full or semi-filled external electron structure, and trapped electrons cannot generate excitons because they are bound by surface oxygen defects [48]. Therefore, the PL intensity decreased. In particular, the $CaTiO_3$@Ni-Pt catalyst showed the lowest PL intensity. Thus, it was suggested that the loading of pure $CaTiO_3$ with Ni and Pt may slow down the recombination between excitons and holes and may play an important role in increasing the photocatalytic efficiency. In addition, the photocurrent response results are shown in Fig. 9(B) to compare the charge separation between the excited electrons and holes. The photocurrent value when the light was irradiated was measured by adjusting the switch of the light source at 30 s intervals. When the electrons were excited by the irradiated light, electron/hole pairs were generated. Their charge separation and electron mobilities were closely related to the photocurrent values [49]. The photocurrent densities of all catalysts showed excellent stability and reliability. Photocurrent density values were increased as follows: $CaTiO_3 < CaTiO_3$@Ni $< CaTiO_3$@Ni-Pt. Thus, the band-gap was reduced by the loaded Ni and Pt, and could promote more light absorption and charge separation, leading to a positive effect on catalytic activity in photo-thermal hybrid reactions. Based on these optical properties, we measured the quantum efficiency of the $CaTiO_3$@Ni-Pt catalyst under photo-thermal hybrid conditions. The quantum efficiency was measured at 40 °C intervals with simultaneous irradiation of heat and light with a wavelength of 365 nm. The results are shown in Fig. 9 **(C)**. Quantum efficiency (QE) was calculated using the following equation (6) based on the 1 sun (100 mW/cm^2) reference.

$$\text{Sample QE} = (\text{sample } J_{sc}/\text{reference } J_{sc}) \times \text{reference QE} \quad (6)$$

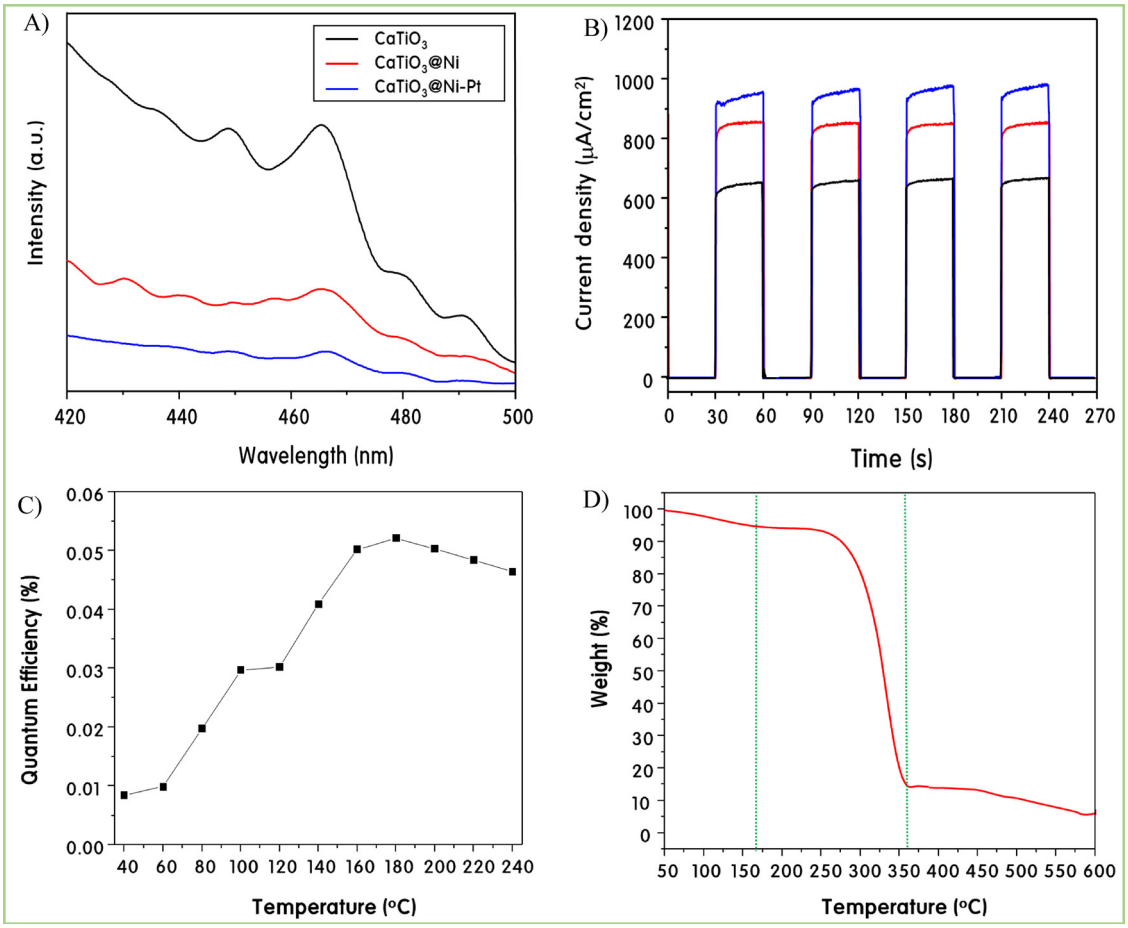

Fig. 9. (A) PL spectra and (B) photocurrent responses of all catalysts, (C) quantum efficiency of $CaTiO_3$@Ni-Pt, and (D) TPO results of the I_3/I^- electrolyte.

The recombination speed of the photo-generated electrons and holes pairs affects the quantum efficiency. The faster the recombination rate, the lower the quantum efficiency [50]. Quantum efficiency increased under photo-thermal hybrid conditions compared to photo-conditions alone. In particular, the quantum efficiency reached its highest at approximately 180 °C, and decreased at higher temperatures. We performed TPO measurements for the electrolyte as shown in Fig. 9(D) because the electrolyte may be decreasing the quantum efficiency at high temperatures. However, the electrolyte was stable up to 350 °C. Therefore, the optimum temperature for synergy was approximately 180 °C, and the heat effect was expected to be greater than the light effect at higher temperatures.

3.5. CO_2 photo-thermal reduction over $CaTiO_3$, $CaTiO_3$@Ni, and $CaTiO_3$@Ni-Pt catalysts

Based on various characteristics of the catalyst, the CO_2 conversion reaction was performed under four conditions. Usually, the reaction conditions in the CO_2 photo-reduction and CO_2 thermal-methanation are different. Generally, the CO_2 photo-reduction reaction using CO_2 and H_2O does not require pre-reducing the catalyst. Furthermore, the thermal CO_2 methanation which uses CO_2 and H_2 mostly utilizes a catalyst pretreated by hydrogen reduction. Therefore, we analyzed four types of reactions in Fig. 10:(A) CO_2 photo-thermal hybrid reaction with H_2O and H_2 over reduced catalysts, (B) CO_2 photo-methanation with H_2O on non-reduced catalyst, (C) CO_2 thermal-methanation with H_2 on reduced catalyst, and (D) CO_2 photo-thermal hybrid reaction with H_2O and H_2 on non-reduced catalyst. First, Fig. 10(A) shows the productions of CO and CH_4 during the CO_2 photo-thermal hybrid reaction for the pre-treated catalysts. Table 2 summarizes the CO conversion and the CO and CH_4 selectivities of the catalysts, depending on temperature. The $CaTiO_3$ used as a support did not show any noticeable performance improvement under light and heat irradiation compared to light irradiation alone. The conversion of CO_2 was maximal at 16.42%, the performance was low at 1 μL of detected CO and CH_4 product, and the product ratio was nonselective. In particular, the amount of gas detected by gas chromatography (GC) was very low compared to the amount of CO_2 consumed. It mean that intermediates such as CH_3OH and HCOOH [51], which could be generated before reduction to CO or CH_4 in the CO_2 reduction process, were produced but were not detected by GC. However, the catalytic performances of the $CaTiO_3$@Ni and $CaTiO_3$@Ni-Pt catalysts were improved under photo-thermal conditions. The conversions of the $CaTiO_3$@Ni and $CaTiO_3$@Ni-Pt catalysts were 29.16 and 46.48%, respectively, and the selectivity for CH_4 production was significantly increased in both catalysts. Up to 100 °C, the products were mixed with CO and CH_4 similar to the results obtained for $CaTiO_3$. However, at 100 °C or higher temperatures, the selectivity of CO dropped under 10%, confirming that only CH_4 was produced. These results meant that Ni and Pt acted as catalytically active sites and the CO_2 methanation on $CaTiO_3$@Ni and $CaTiO_3$@Ni-Pt were mediated by the photo-thermal synergy effect rather than photocatalytic action. In particular, $CaTiO_3$@Ni-Pt showed the most rapid increase in CH_4 production from 160 °C, which was consistent with the measurements of quantum efficiency under photo-thermal conditions. According to the existing literature, a temperature of 200 °C or more is required for an effective CO_2 thermal-methanation reaction [52]. Compared with the general thermal reaction, the present study confirmed the possibility that the temperature required for CO_2 methanation in the photo-thermal system can be lower. On the other hand, Fig. 10(B) displayed the CO_2 photo-reduction with H_2O on non-

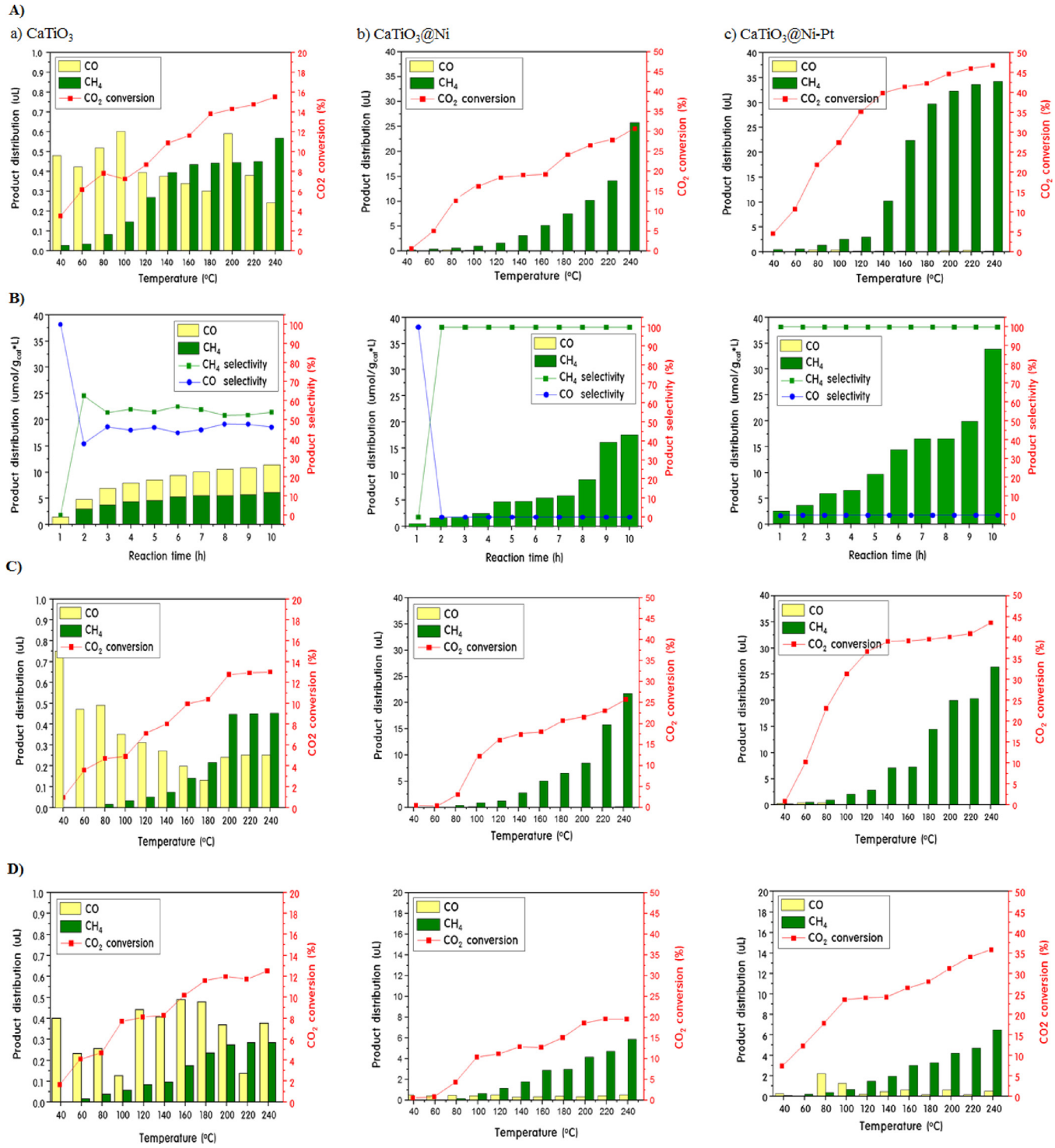

Fig. 10. (A) Catalytic performances of CO_2 photo-thermal hybrid reaction with H_2O and H_2 over reduced catalysts, (B) CO_2 photo-methanation with H_2O on non-reduced catalyst, (C) CO_2 thermal-methanation with H_2 on reduced catalyst, and (D) CO_2 photo-thermal hybrid reaction with H_2O and H_2 on non-reduced catalyst.

reduced catalyst. The photoreaction was carried out in a closed system because it was difficult to perform in a continuous system. Therefore, it is shown as the amount of product produced over time, and only the main products, methane and CO, are presented. As shown in Fig. 12, a small amount of CH_3OH was measured in Mass spectroscopy, but it was not observed in GC and was not included in the quantitative analysis. Unlike the thermal reaction, the amount of CO_2 reduction on the $CaTiO_3$ catalyst was small and only 10 μmol of CH_4 and CO were obtained after 10 h. However, as in other systems, the selectivity of CH_4 increased by 3 times (from 6 μmol to 18 μmol) after 10 h when Ni was added. The Ni could activate hydrogen either by reducing H_2 to H^- and then reacting with Ni^+ or by oxidizing H_2 to H^+ and then reacting with Ni^-. This proposal, based on the formation of metal hydrides, is compatible with the observation of CH_4 formation [53]. In particular, the yield of CH_4 on the $CaTiO_3$@Ni-Pt catalyst including Pt largely increased, which was higher 5.5 times than it on $CaTiO_3$. No further CO products were seen in both catalysts. From these results, we have confirmed that the selectivity to CH_4 on the Ni and Pt catalyst is entirely

Table 2
CO conversion, and CO and CH_4 selectivities of the reduced $CaTiO_3$, $CaTiO_3$@Ni, and $CaTiO_3$@Ni-Pt catalysts during the CO_2 photo-thermal hybrid reaction as functions of the reaction temperatures.

Cats.	$CaTiO_3$			$CaTiO_3$@Ni			$CaTiO_3$@Ni-Pt		
Temp. (°C)	CO_2	CO	CH_4	CO_2	CO	CH_4	CO_2	CO	CH_4
40	4.41	94.56	5.44	0.94	16.47	83.53	4.33	19.78	80.22
60	7.05	92.55	7.45	5.35	21.38	78.62	10.42	11.66	88.34
80	8.71	86.10	13.90	16.43	27.69	72.31	21.51	26.28	73.72
100	8.14	80.39	19.61	16.54	15.70	84.30	27.13	14.07	85.93
120	9.58	59.47	40.53	18.75	7.72	92.28	34.84	5.89	94.11
140	11.77	48.70	51.30	19.32	3.36	96.64	39.50	1.90	98.10
160	12.53	43.73	56.27	19.52	1.92	98.07	41.12	0.92	99.08
180	14.71	40.52	59.48	28.90	1.04	98.96	41.95	0.54	99.46
200	15.19	57.06	42.94	28.59	0.11	99.89	44.36	0.80	99.20
220	15.66	45.71	54.29	29.26	0.29	99.71	45.70	1.19	98.81
240	16.42	29.86	70.14	29.71	0.06	99.94	46.48	0.54	99.46

CO_2: Conversion, CO and CH_4: Selectivity.

dominant in the photoreaction. In particular, the reason why the Pt addition into the catalyst increases the catalytic performance, and in particular, the selectivity to CH_4 increases can be explained by two factors. The first is that the Pt helps the H_2 generated by decomposing the H_2O injected by the CO_2 as a reducing agent, and the second is that the adsorption of H_2 on the Pt occurs well (the factor is described in Fig. 10 (D)). As the first factor, many researchers have already reported [54,55] that water decomposition readily occurs on Pt/TiO_2 catalysts, thereby promoting H_2 production. Especially, Yu et al. reported [56] that the Pt nanoparticle on TiO_2 produces a Schottky barrier, which facilitates the electron capture. Accumulation of holes at the valence band of TiO_2 leads to the production of surface hydroxyl radical •OH. Photogenerated electrons are effectively accumulated on Pt nanocrystal particles without recombining with holes. This causes a significant enhancement of the photocatalytic activity in H_2 production. Meanwhile, Fig. 10(C) presented the CO_2 photo-reduction with H_2O on non-reduced catalyst. In general, the thermal methanation of CO_2 using H_2 as a reducing agent starts to be activated at 200 °C, and the conversion rate of CO_2 reaches almost 100% at about 300 ~ 500 °C, where the CH_4 yield is also 90% or more. Optimal thermodynamic equilibrium is achieved around these temperatures, but when the reaction temperature is above 500 °C, the equilibrium is collapsed and the conversion of CO_2 drops gradually [57,58]. However, since this study must harmonize with the photo system, the reaction temperature did not rise above 240 °C, and it was confirmed that the quantum efficiency decreased when the temperature was raised above 180 °C in Fig. 9. Therefore, the reaction temperature was too low to reach the thermal equilibrium for CO_2 methanation, resulting in low conversion of CO_2, resulting in low CH_4 and CO productions. But, the amounts of products in the thermal reaction were much higher than in the photoreaction. Moreover, 25 μL of CH_4 production at 240 °C on a $CaTiO_3$@Ni-Pt catalyst is considered to be an almost ideal amount, considering the conversion of CO_2. Unusual is that the amount of CO generated in $CaTiO_3$ is very high, which means that the rate of CO_2 to CO in the thermal reaction is very fast. Nevertheless, the fact that the amount of CH_4 obtained is small suggests that in the end of the thermal reaction, CO hydrogenation (CO → CH_4) requires a higher temperature than this temperature. Finally, the CO_2 photo-thermal hybrid reaction with H_2O and H_2 on non-reduced catalyst was seen in Fig. 10(D). The results were quite different compared to the results of (A), although the treatment of the catalyst was different and the system was the same. There seem to be two factors here. The first is the difference in H_2 (also hydrogen like) adsorption capacity for the catalyst. In general, H_2 is better adsorbed on the metallic or alloy component Ni-Pt than on the NiO-Pt [59,60]. Therefore, in the (A) system, on the Ni-Pt of the $CaTiO_3$@Ni-Pt catalyst, H_2 was well adsorbed, and the CO_2 methanation by the thermal reaction taken priority, but the adsorption of H_2 did not occur on the catalyst in the unreduced (D) system, thus the CO_2 methanation occurred by photo. As already mentioned, the difference in the yields of CO_2 methanization of the photoreaction and the thermal reaction is very large and much more CH_4 is generated in the thermal CO_2 reduction reaction. The second is that the difference in crystallinity of the reduced catalyst seems to have changed the performance. ABO_3 materials with a perovskite structure are cubic structures that can easily make oxygen defects. When the A or B is doped with other elements [61] or treated with hydrogen [62], existing oxygen vacancies become empty or new oxygen enters into the oxygen vacancy site. The oxygen vacancies can promote reaction gas adsorption by extending the reaction site of the catalyst. In XPS results of Fig. 8, we confirmed that oxygen vacancy was partially formed in $CaTiO_3$ with addition of Ni and Pt. However, it is believed that its influence is less than the influence of oxygen vacancy caused by the hydrogen treatment on the catalytic performance. Therefore, oxygen vacancies are expected to be generated more reliably by hydrogen treatment. As a result, the catalyst used in (A) system was treated with hydrogen, resulting in an oxygen vacancy in $CaTiO_3$, which promoted the adsorption of CO_2, and this adsorbed CO_2 could easily escape to CO by leaving O in the oxygen vacancy. Thus, it is possible to lower the activation energy of the rate determining step for generating CO in the process. However, this effect was not obtained with catalysts which did not undergo any treatment in (D) system, and

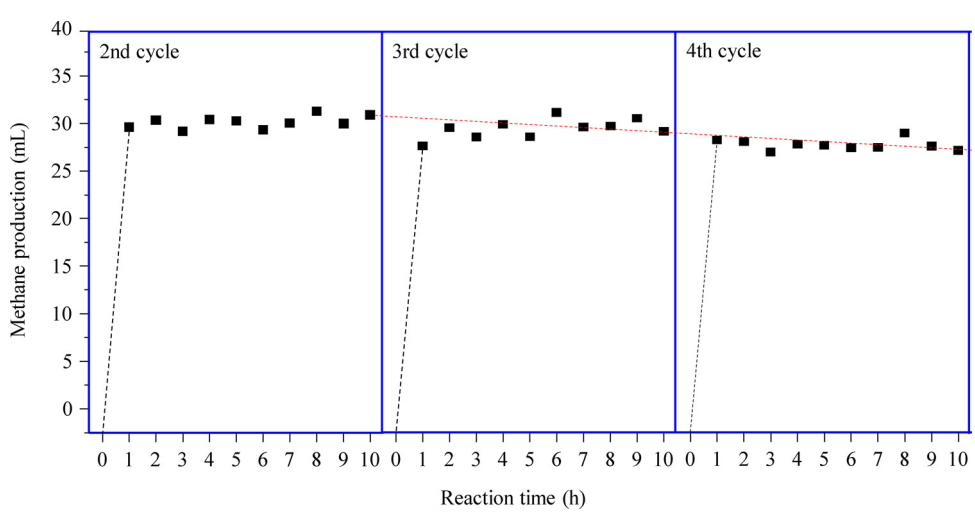

Fig. 11. Recycling tests for the photo-thermal stability of $CaTiO_3$@Ni-Pt catalyst during photo-thermal reaction (at 180 °C).

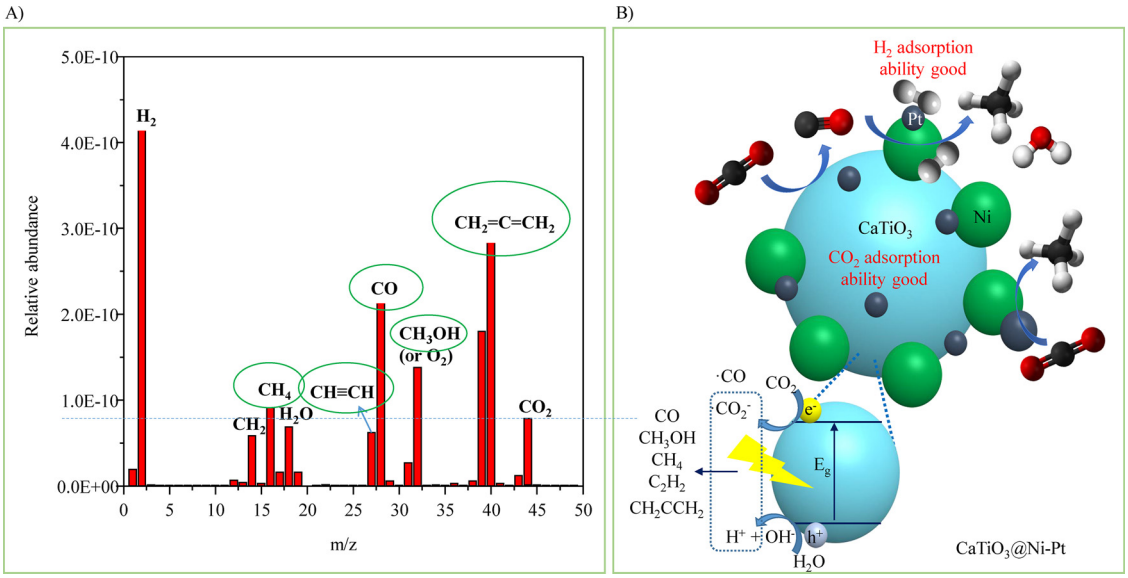

Fig. 12. (A) Mass spectroscopy analysis and (B) an expected mechanisms during the CO_2 photo-thermal hybrid reaction on the $CaTiO_3$@Ni-Pt catalyst.

as a result the performance on CO_2-methanation was poor.

Fig. 11 shows the results on recycling tests for the photo-thermal stability of $CaTiO_3$@Ni-Pt catalyst during the photo-thermal reaction (at 180 °C exhibiting the best quantum efficiency). Catalyst regeneration was carried out as follows: The catalyst used was separated from the photo-thermal system in a state in which it remained packed in the column. This is transferred to another thermal reactor and buried, and calcined at 500 °C for 2 h while a flowing of air to remove impurities adhering to the surface. As a next step, the catalyst was reduced under H_2 flow (10 mL/min) for 1 h at the same temperature. The column containing the reduced catalyst is re-mounted in the photo-thermal system and the temperature is raised at a rate of 10 °C/min to 180 °C with purging of N_2. After stabilizing the temperature for 1 h at 180 °C, the CO_2 methanation is performed for 10 h while injecting a certain amount of CO_2 gas, H_2 gas, and H_2O vapor. The reaction time per cycle was 10 h. After one cycle, the catalyst regeneration process was repeated. Three cycles were repeated and the amount of CH_4 generated on reaction time was presented. The amount of CH_4 produced in the 1st-cycle of Fig. 10(A), which was about 30 μL, did not differ significantly from 29 to 31 μL in the 2nd-cycle of Fig. 11. A little unusual is that, unlike ordinary photo or thermal reactions, the amount of CH_4 generated over time is not constant but occurs in a zigzag type. This phenomenon is often seen in plasma reactions, presumably as a mixture of photo-thermal energy, acting like plasma. In the 3rd-cycle, the change in CH_4 production did not appear to be significant, but the amount of CH_4 production began to decrease to 27 μL on the 4th-cycle. This is presumably due to the reduction of the catalytic active sites by sintering of the Ni component present in the $CaTiO_3$@Ni-Pt catalyst. It is considered that the deterioration has progressed more rapidly due to repetitive treatment of hydrogen and oxygen during the regeneration process in this study. Fortunately, the decrease in CH_4 was not large.

A mass spectrometer was used to observe all the intermediates in the CO_2 photo-thermal hybrid reaction using $CaTiO_3$@Ni-Pt, which had the best performance, and the results are shown in Fig. 12 (A). An expected mechanism of the CO_2 photo-thermal reaction for $CaTiO_3$@Ni-Pt based on the catalytic performance, physicochemical properties, and especially mass spectroscopy of the CO_2 photo-thermal hybrid reaction is shown in Fig. 12(B). Mass spectrometry during the CO_2 photo-thermal hybrid reaction confirmed the presence of CO and CH_4, as well as CH_2 and CH_3OH, which were not detected by GC. These results indicated that CO_2 adsorbed by the $CaTiO_3$ photocatalyst used as a support produced intermediate CO and CH_3OH by light irradiation, and these intermediates are rapidly reduced to CH_4 by the Ni and Pt active species. That is, the CO_2 and H_2O molecules were preferentially adsorbed on the surface of the $CaTiO_3$ support. Both CO and H_2 could be generated by the photoreduction of CO_2 and H_2O on $CaTiO_3$@Pt. Generally, CO_2 adsorbed on the metal surface undergoes decomposition reactions at temperatures lower than 100 °C to produce CO ($CO_{2\ ads} \rightarrow CO_{ads} + O_{ads}$) as an intermediate of CO_2 methanation [63]. The process of reducing CO_2 to CO is considered a rate determining step. At this time, successive CO methanation processes ($CO + 3H_2 \rightarrow CH_4 + H_2O$) [64] could be promoted by Ni and Pt, which had high methanation ability and hydrogen adsorption/spillover ability. As a result, higher CH_4 amounts were obtained compared to the conventional photo-methanation process. Here, let's approach more detail the mechanism for CO_2 methanation. The H_2O injected in the photo-reaction or photo-thermal reaction is very important as a reducing agent of CO_2. The two molecules of H_2O vapor are adsorbed on the $CaTiO_3$@Ni-Pt catalyst, and when the photocatalyst absorbs light, it decomposes into $2H^+$ and 2•OH at the hole of the VB of $CaTiO_3$. The $2H^+$ is converted to H_2 by receiving excited electrons on the CB, and the H_2 is adsorbed on Ni-Pt (here preferentially over Pt rather than Ni) until participating in the reaction. On the other hand, the 2•OH is decomposed into O_2 and $2H^+$ on the hole of VB, and the $2H^+$ is converted to H_2 by receiving electrons as above. The O_2 exits as a product, or it receives electrons from the CB, passes through O_2^-, then converts to H_2O_2 by combining with H_2O, and then decomposes into 2•OH by light. Thus, H_2O ultimately produces H_2 and O_2, but by photolysis it can produce intermediates such as H^+, $\cdot O_2^-$, ·OH, H_2O_2, and so on [65]. On the other hand, regardless of the H_2 generated from the H_2O or the H_2 injected from the outside, all the H_2 are adsorbed on the Ni-Pt and then decomposed to 2H· under light irradiation. They are converted to H^- by the electron from the CB of $CaTiO_3$ and oxidized to H^+ at the hole of the VB. In particular, the H^- made on CB is adsorbed as H-Pt-Ni state, and reacts with CO_2 and changes into HCO_2-Pt-Ni. Finally, the HCO intermediate is formed by the CO_2 hydrogenation reaction, and CH_4 is formed by passing $C \rightarrow CH \rightarrow CH_2 \rightarrow CH_3$, step by step. At this time, the reactant, CO_2, is adsorbed on the CaO of $CaTiO_3$ into the form of $CaCO_3$, moves along the surface of the catalyst, and reacts with $4H^-$ on Ni to generate CH_4. The H^+ generated from VB can also take electrons and participate in the same reaction [66]. On the other hand, two new products, C_2H_2 (acetylene) and CH_2CCH_2 (allene), non-observed in photo- or thermo- reactions, were observed in photo-thermal hybrid system. A small amount of CH_4 produced carbon dimer, carbon, and carbon trimmer, which are derived

from methane via the Reactions, [7]–[9].

$$2CH_4 + \Delta + hv \rightarrow C_2H_2 + 3H_2 \quad (7)$$

$$CH_4 + \Delta + hv \rightarrow C + 2H_2 \quad (8)$$

$$C_2H_2 + C + \Delta + hv \rightarrow CH_2CCH_2 \quad (9)$$

Judging from the fact that the synthesis products generated in the plasma system are observed in the photo-thermal hybrid system [67], the photo-thermal energy in the photo-thermal hybrid system is presumably assumed to act like the plasma. It is believed that the powerful energy generated in the plasma eventually results in the generation of strong intermediate radicals at the intermediate stage and thereby accelerates the product. Recently, Chen et al. reported that the CoFe-x catalysts showed a progressive selectivity shift from CO to CH_4 in photo-thermal CO_2 Hydrogenation, and eventually to high-value hydrocarbons (C_{2+}) with increasing the reduction temperature. They confirmed the key role of the CoFe alloy structure in promoting C—C coupling reactions during CO_2 hydrogenation by the DFT calculations [68]. But, it has not yet been revealed whether the intermediate radicals are a carbon, a hydrocarbon or a CO radical. Furthermore, they were obtained at a lower temperature than the conventional thermo-methanation process. However, since the C_2H_2 and CH_2CCH_2 products were rarely measured with GC detectors (perhaps because our experimental target was CH_4 and we used a GC detector fitted to CH_4, other hydrocarbons might have lower sensitivity), thus they were excluded from the product distributions of Table 2.

4. Conclusions

This research attempted to develop a catalyst applicable to new photo-thermal hybrid systems to efficiently convert CO_2 to CH_4. In this study, we tried to improve the amounts of CH_4 obtained during conventional photo conversion reactions, to partially replace H_2 with H_2O during the thermal conversion and to lower the reaction temperature. We introduced a $CaTiO_3$@Ni-Pt catalyst, which has both thermo- and photo-catalytic activities. The catalyst adsorbed/desorbed higher amounts of CO_2 and H_2 gases at lower temperatures compared to $CaTiO_3$. The performance of the $CaTiO_3$@Ni-Pt catalyst was improved as it demonstrated 46.48% CO_2 conversion and 99.46% CH_4 selectivity at 180 °C. The photoluminescence and photocurrent results proved that the recombination of the charges photo-generated by Ni and Pt was suppressed, which could improve catalytic activity. In photo-thermal hybrid systems, the catalytic quantum efficiency steadily increased up to 180 °C, however, it decreased at higher temperatures. These results implied that the optimum temperature for photo-thermal synergy, indicating the best catalytic performance, was approximately 180 °C.

Acknowledgments

This work was conducted under framework of the research and development program of the Korea Institute of Energy Research (B8-2437), and this work was also supported by the Korea Institute of Energy Technology Evaluation and Planning (KETEP) and the Ministry of Trade, Industry and Energy (MOTIE) of the Republic of Korea (No. 20163010050080), and the authors are grateful it.

References

[1] R.M. Cuellar-Franca, A. Azapagic, Carbon capture, storage and utilization technologies: a critical analysis and comparison of their life cycle environmental impacts, J. CO_2 Util. 9 (2015) 82–102.
[2] A. Al-Mamoori, A. Krishnamurthy, A.A. Rownaghi, F. Rezaei, Carbon capture and utilization update, Energy Technol. 5 (2017) 834–849.
[3] J.Y. Do, Y. Im, B.S. Kwak, J. Kim, M. Kang, Dramatic CO_2 photoreduction with H_2O vapors for CH_4 production using the TiO_2 (bottom)/Fe–TiO_2 (top) double-layered films, Chem. Eng. J. 275 (2015) 288–297.
[4] K. Li, X. An, K.H. Park, M. Khraisheh, J. Tang, A critical review of CO_2 photoconversion: catalysts and reactors, Catal. Today 224 (2014) 3–12.
[5] J. Xu, X. Su, H. Duan, B. Hou, Q. Lin, X. Liu, X. Pan, G. Pei, H. Geng, Y. Huang, T. Zhang, Influence of pretreatment temperature on catalytic performance of rutile TiO_2-supported ruthenium catalyst in CO_2 methanation, J. Catal. 333 (2016) 227–237.
[6] J.N. Park, W. McFarland, A highly dispersed Pd–Mg/SiO_2 catalyst active for methanation of CO_2, J. Catal. 266 (2009) 92–97.
[7] E.T. Kho, T.H. Tan, E. Lovell, R.J. Wong, J. Scott, R. Amal, A review on photo-thermal catalytic conversion of carbon dioxide, Green. Energy Environ. 2 (2017) 204–217.
[8] A. Primo, A. Corma, H. Garcia, Titania supported gold nanoparticles as photocatalyst, Phys. Chem. Chem. Phys. 13 (2011) 886–910.
[9] A.O. Ibhadon, P. Fitzpatrick, Heterogeneous photocatalysis: recent advances and applications, Catalysis 3 (2013) 189–218.
[10] H. Suzuki, M. Sugimoto, Y. Matsui, J. Kondoh, Effects of gold film thickness on spectrum profile and sensitivity of a multimode-optical-fiber SPR sensor, Sens. Actuat. B-Chem. 132 (2008) 26–33.
[11] Z. Zhang, W. Wang, E. Gao, S. Sun, L. Zhang, Photocatalysis coupled with thermal effect induced by SPR on Ag-loaded Bi_2WO_6 with enhanced photocatalytic activity, J. Phys. Chem. C. 116 (2012) 25898–25903.
[12] W. Yang, Y. Xiong, L. Zou, Z. Zou, D. Li, Q. Mi, Y. Wang, H. Yang, Plasmonic Pd nanoparticle- and plasmonic Pd nanorod-decorated $BiVO_4$ electrodes with enhanced photoelectrochemical water splitting efficiency across visible-NIR region, Nanoscale Res. Lett. 11 (2016) 283–2910.
[13] B.S. Kwak, M. Kang, Photocatalytic reduction of CO_2 with H_2O using perovskite $Ca_xTi_yO_3$, Appl. Surf. Sci. 337 (2015) 138–144.
[14] P.S. Whitfield, N. Herron, W.E. Guise, K. Page, Y.Q. Cheng, I. Milas, M.K. Crawford, Structures, phase transitions and tricritical behavior of the hybrid perovskite methyl ammonium lead iodide, Sci. Rep. 6 (2016) 35685–35701.
[15] G. Peng, S.J. Sibener, G.C. Schatz, M. Mavrikakis, CO_2 hydrogenation to formic acid on Ni (110), Surf. Sci. 606 (2012) 1050–1055.
[16] K. Ray, G. Deo, A potential descriptor for the CO_2 hydrogenation to CH_4 over Al_2O_3 supported Ni and Ni-based alloy catalysts, Appl. Catal. B. 218 (2017) 525–537.
[17] P. Panagiotopoulou, Hydrogenation of CO_2 over supported noble metal catalysts, Appl. Catal. A. 542 (2017) 63–70.
[18] S.M. Kozlov, H.A. Aleksandrov, K.M. Neyman, Energetic stability of absorbed H in Pd and Pt nanoparticles in a more realistic environment, J. Phys. Chem. C. 119 (2015) 5180–5186.
[19] L.L. Hench, J.K. West, The sol-gel process, Chem. Rev. 90 (1990) 33–72.
[20] S. Jung, C. Lu, H. He, K. Ahn, R.J. Gorte, J.M. Vohs, Influence of composition and Cu impregnation method on the performance of Cu/CeO_2/YSZ SOFC anodes, J. Power Sources 154 (2006) 42–50.
[21] H. Jeong, M. Kang, Hydrogen production from butane steam reforming over Ni/Ag loaded $MgAl_2O_4$ catalyst, Appl. Catal. B. 95 (2010) 446–455.
[22] G. Dong, X. Xiao, L. Zhang, Z. Ma, X. Bao, M. Peng, Q. Zhang, J. Qiu, Preparation and optical properties of red, green and blue afterglow electrospun nanofibers, J. Mater. Chem. 21 (2011) 2194–2203.
[23] M. El-Kemary, N. Nagy, I. El-Mehasseb, Nickel oxide nanoparticles: synthesis and spectral studies of interactions with glucose, Mater. Sci. Semicond. Process. 16 (2013) 1747–1752.
[24] A.W. Burton, K. Ong, T. Rea, I.Y. Chan, On the estimation of average crystallite size of zeolites from the Scherrer equation: a critical evaluation of its application to zeolites with one-dimensional pore systems, Micropor. Mesopor. Mater. 117 (2009) 75–90.
[25] Y. Dahmane, L. Cagnon, J. Voiron, S. Pairis, M. Bacia, L. Ortega, N. Benbrahim, A. Kadri, Magnetic and structural properties of electrodeposited CoPt and FePt nanowires in nanoporous alumina templates, J. Phys. D: Appl. Phys. 39 (2006) 4523–4528.
[26] F. Wang, Z. Wen, C. Shen, K. Rui, X. Wu, C. Chen, Open mesoporous spherical shell structured Co_3O_4 with highly efficient catalytic performance in Li–O_2 batteries, J. Mater. Chem. A 3 (2015) 7600–7606.
[27] H. Lin, C.P. Huang, W. Li, C. Ni, S. Ismat Shah, Y.H. Tseng, Size dependency of nanocrystalline TiO_2 on its optical property and photocatalytic reactivity exemplified by 2-chlorophenol, Appl. Catal. B. 68 (2006) 1–11.
[28] R. Pol, M. Guerrero, E.G. Lecina, A. Altube, E. Rossinyol, S. Garroni, M.D. Baró, J. Pons, J. Sort, E. Pellicer, Ni-, Pt- and (Ni/Pt)-doped TiO_2 nanophotocatalysts: a smart approach for sustainable degradation of Rhodamine B dye, Appl. Catal. B. 181 (2016) 270–278.
[29] N. Son, J.Y. Do, M. Kang, Characterization of core@shell-structured ZnO@Sb_2S_3 particles for effective hydrogen production from water photo splitting, Ceram. Int. 43 (2017) 11250–11259.
[30] Y. Zhao, Y. Wei, X. Wu, H. Zheng, Z. Zhao, J. Liu, J. Li, Graphene-wrapped Pt/TiO_2 photocatalysts with enhanced photogenerated charges separation and reactant adsorption for high selective photoreduction of CO_2 to CH_4, Appl. Catal, B. 226 (2018) 360–372.
[31] X. Meng, T. Wang, L. Liu, S. Ouyang, P. Li, H. Hu, T. Kako, H. Iwai, A. Tanaka, J. Ye, Photothermal conversion of CO_2 into CH_4 with H_2 over group VIII nanocatalysts: an alternative approach for solar fuel production, Angew. Chem. 126 (2014) 11662–11666.
[32] F. Song, Q. Zhong, Y. Yu, M. Shi, Y. Wu, J. Hu, Y. Song, Obtaining well-dispersed Ni/Al_2O_3 catalyst for CO_2 methanation with a microwave-assisted method, Int. J. Hydrog. Energy 42 (2017) 4174–4183.
[33] J.Y. Do, J.H. Lee, N.K. Park, T.J. Lee, S.T. Lee, M. Kang, Synthesis and characterization of $Ni_{2-x}Pd_xMnO_4/\gamma$-Al_2O_3 catalysts for hydrogen production via propane steam reforming, Chem. Eng. J. 334 (2018) 1668–1678.
[34] B.S. Kwak, K.M. Kim, S.W. Jo, J.Y. Do, S. Kang, M. Park, N.K. Park, T.J. Lee,

S.T. Lee, M. Kang, Characterizations of bimetallic NiV-supported SiO_2 catalysts prepared for effectively hydrogen evolutions from ethanol steam reforming, J. Ind. Eng. Chem. 37 (2016) 57–66.
[35] A. Song, G. Lu, Enhancement of Pt–Ru catalytic activity for catalytic wet air oxidation of methylamine via tuning the Ru surface chemical state and dispersion by Pt addition, RSC Adv. 4 (2014) 15325–15331.
[36] A. Smirnov, D. Hausner, R. Laffers, D.R. Strongin, M.A.A. Schoonen, Abiotic ammonium formation in the presence of Ni-Fe metals and alloys and its implications for the Hadean nitrogen cycle, Geochem. Trans. 9 (2008) 1–20.
[37] C.L. Mangun, M.A. Daley, R.D. Braatz, J. Economy, Effect of pore size on adsorption of hydrocarbons in phenolic-based activated carbon fibers, Carbon 36 (1998) 123–131.
[38] M. Thommes, K. Kaneko, A.V. Neimark, J.P. Olivier, F.R. Reinoso, J. Rouquerol, K.S.W. Sing, Physisorption of gases, with special reference to the evaluation of surface area and pore size distribution (IUPAC technical report), Pure Appl. Chem. (2015) 1–19.
[39] D. Li, K. Nishida, Y. Zhan, T. Shishido, Y. Oumi, T. Sano, K. Takehira, Superior catalytic behavior of trace Pt-doped Ni/Mg(Al)O in methane reforming under daily start-up and shut-down operation, Appl. Catal. A. 350 (2008) 225–236.
[40] Y. Im, S.M. Park, M. Kang, Effect of Ca/Ti ratio on the core–shell structured $CaTiO_3$@basalt fiber for effective photoreduction of carbon dioxide, Bull. Korean Cem. Soc. 38 (2017) 397–400.
[41] J. Jia, C. Qian, Y. Dong, Y.F. Li, H. Wang, M. Ghoussoub, K.T. Butler, A. Walsh, G.A. Ozin, Heterogeneous catalytic hydrogenation of CO_2 by metal oxides: defect engineering – perfecting imperfection, Chem. Soc. Rev. 46 (2017) 4631–4644.
[42] H. Tan, F. Zou, B. Ma, M. Liu, X. Li, S. Jian, Effect of sodium tripolyphosphate on adsorbing behavior of polycarboxylate superplasticizer, Constr. Build. Mater. 126 (2016) 617–623.
[43] S.K.M. Saad, A.A. Umar, M.I.A. Umar, M. Tomitori, M.Y.A. Rahman, M.M. Salleh, M. Oyama, Two-dimensional, hierarchical Ag-doped TiO_2 nanocatalysts: effect of the metal oxidation state on the photocatalytic properties, ACS Omega 3 (2018) 2579–2587.
[44] D.H. Wang, L. Jia, X.L. Wu, L.Q. Lu, A.W. Xu, One-step hydrothermal synthesis of N-doped TiO_2/C nanocomposites with high visible light photocatalytic activity, Nanoscale 4 (2012) 576–584.
[45] V.G. Prabhu, A.R. Paloly, N.G. Divya, M.J. Bushiri, Photocatalytic and ferromagnetic properties of electrically conducting multifunctional Ni/NiO nanocomposites in amorphous carbon matrix, Mater. Sci. Eng. B 228 (2018) 132–141.
[46] M.A. Main, E. Lee, H. Kim, W.S. Yoon, Y.U. Kwon, Rational syntheses of core–shell Fe@(PtRu) nanoparticle electrocatalysts for the methanol oxidation reaction with complete suppression of CO-poisoning and highly enhanced activity, J. Mater. Chem. A. 3 (2015) 17154–17164.
[47] D. Wojcieszak, D. Kaczmarek, J. Domaradzki, M. Mazur, Correlation of photocatalysis and photoluminescence effect in relation to the surface properties of TiO_2:Tb thin films, Int. J. Photoenergy (2013) (2013) 1–9.
[48] F. Mehmood, J. Iqbal, M. Ismail, A. Mehmood, Ni doped WO_3 nanoplates: an excellent photocatalyst and novel nanomaterial for enhanced anticancer activities, J. Alloy Compd. 746 (2018) 729–738.
[49] V. Pranculis, Y. Infahsaeng, Z. Tang, A. Devižis, D.A. Vithanage, C.S. Ponseca Jr, O. Inganäs, A.P. Yartsev, V. Gulbinas, V. Sundström, Charge carrier generation and transport in different stoichiometry $APFO_3$:$PC_{61}BM$ solar cells, J. Am. Chem. Soc. 136 (2014) 11331–11338.
[50] B. Ohtani, Photocatalysis A to Z—what we know and what we do not know in a scientific sense, J. Photochem. Photobiol. C 11 (2010) 157–178.
[51] L. Liu, Y. Li, Understanding the reaction mechanism of photocatalytic reduction of CO_2 with H_2O on TiO_2-based photocatalysts: a review, Aerosol Air Qual. Res. 14 (2014) 453–469.
[52] E.T. Kho, S. Jantarang, Z. Zheng, J. Scott, R. Amal, Harnessing the beneficial attrivutes of ceria and titania in a mixed-oxide support for nickel-catalyzed photothermal CO_2 methanation, Engineering 3 (2017) 393–401.
[53] F. Sastre, A.V. Puga, L. Liu, A. Corma, H. García, Complete photocatalytic reduction of CO_2 to methane by H_2 under solar light irradiation, J. Am. Chem. Soc. 136 (2014) 6798–6801.
[54] Y. Yang, C. Chang, H. Idriss, Photo-catalytic production of hydrogen form ethanol over M/TiO_2 catalysts (M = Pd, Pt or Rh), Appl. Catal. B 67 (2006) 217–222.
[55] Á. Kmetykó, K. Mogyorósi, V. Gerse, Z. Kónya, P. Pusztai, A. Dombi, K. Hernádi, Photocatalytic H_2 production using Pt-TiO_2 in the presence of cxalic acid: influence of the noble metal size and the carrier gas flow rate, Material 7 (2014) 7022–7038.
[56] J. Yu, L. Qi, M. Jaroniec, Hydrogen production by photocatalytic water splitting over Pt/TiO_2 nanosheets with exposed (001) facets, J. Phys. Chem. C 114 (2010) 13118–13125.
[57] Kim S, Y. Yoo, S. Kang, J. Ryu, J. Kim, M. Kim, D. Koh, H. Lee, G. Kim, H. Kim, Operating characteristics of a 0.25 MW methanation pilot plant with isothermal reactor and adiabatic reactor, Clean. Technol. 19 (2) (2013) 156–164.
[58] M. Götz, A.M. Koch, F. Graf, State of the art and perspectives of CO_2 methanation process concepts for power-to-gas applications, Int. Gas Union Res. Conf. Copenhagen, 2014 Abstract ID: 325.
[59] J. Greeley, M. Mavrikakis, Surface and subsurface hydrogen: adsorption properties on transition metals and near-surface alloys, J. Phys. Chem. B 109 (2005) 3460–3471.
[60] R. Panta, V. Ruangpornvisuti, Adsorption of hydrogen molecule on noble metal doped on oxygen-vacancy defect of anatase TiO_2 (101) surface: periodic DFT study, Int. J. Hydrogen Energy 42 (2017) 19106–19113.
[61] H. Tan, Z. Zhao, W.-b. Zhu, E.N. Coker, B. Li, M. Zheng, W. Yu, H. Fan, Z. Sun, Oxygen vacancy enhanced photocatalytic activity of pervoskite $SrTiO_3$, ACS Appl. Mater. Interf. 6 (2014) 19184–19190.
[62] J. Zhang, K. Xie, H. Wei, Q. Qin, W. Qi, L. Yang, C. Ruan, Y. Wu, In situ formation of oxygen vacancy in perovskite $Sr_{0.95}Ti_{0.8}Nb_{0.1}M_{0.1}O_3$ (M = Mn, Cr) toward efficient carbon dioxide electrolysis, Sci. Rep. 4 (2014) 7082.
[63] S.J. Choe, H.J. Kang, S.J. Kim, S.B. Park, D.H. Park, D.S. Huh, Adsorbed carbon formation and carbon hydrogenation for CO_2 methanation on the Ni(111) surface: ASED-MO study, Bull. Korean Cem. Soc. 26 (2005) 1682–1688.
[64] J. Barrientos, N. Gonzalez, M. Boutonnet, S. Järås, Deactivation of Ni/γ-Al_2O_3 catalysts in CO methanation: effect of Zr, Mg, Ba and Ca oxide promoters, Top. Catal. 60 (2017) 1276–1284.
[65] L. Liu, Y. Li, Understanding the reaction mechanism of photocatalytic reduction of CO_2 with H_2O on TiO_2-based photocatalysts: a review, Aerosol Air Quality Res. 14 (2014) 453–469.
[66] Y. Zhao, B. Zhao, J. Liu, G. Chen, R. Gao, S. Yao, M. Li, Q. Zhang, L. Gu, J. Xie, X. Wen, L.-Z. Wu, C.-H. Tung, D. Ma, T. Zhang, Oxide-modified nickel photocatalysts for the production of hydrocarbons in visible light, Angew. Chem. Int. Ed. 55 (2016) 4215–4219.
[67] R. Snoeckx, A. Bogaerts, Plasma technology–a novel solution for CO_2 conversion? Chem. Soc. Rev. 46 (2017) 5805–5863.
[68] G. Chen, R. Gao, Y. Zhao, Z. Li, N. Gi, R. Shi, J. Zhao, M. Zhang, L. Shang, G. Sheng, X. Zhang, X. Wen, L.Z. Wu, C.H. Tung, T. Zhang, Alumina-supported CoFe alloy catalysts derived from layered-double-hydroxide nanosheets for efficient photothermal CO_2 hydrogenation to hydrocarbons, Adv. Mater. 30 (3) (2018) 1704663.